Superconductors of finite thickness in a perpendicular magnetic field: Strips and slabs

Ernst Helmut Brandt
Max-Planck-Institut für Metallforschung, Institut für Physik, D-70506 Stuttgart, Germany
(Received 21 March 1996)

The magnetic moment, flux and current penetration, and creep in type-II superconductors of nonzero thickness in a perpendicular applied magnetic field are calculated. The presented method extends previous one-dimensional theories of thin strips and disks to the more realistic case of arbitrary thickness, including as limits the perpendicular geometry (thin long strips and circular disks in a perpendicular field) and the parallel geometry (long slabs and cylinders in a parallel field). The method applies to arbitrary cross section and arbitrary current-voltage characteristics $E(J)$ of conductors and superconductors, but a linear equilibrium magnetization curve $B=\mu_0 H$ and isotropy are assumed. Detailed results are given for rectangular cross sections $2a\times 2b$ and power-law electric field $E(J)=E_c(J/J_c)^n$ versus current density J, which includes the Ohmic ($n=1$) and Bean ($n\to\infty$) limits. In the Bean limit above some applied field value the lens-shaped flux- and current-free core disconnects from the surface, in contrast to previous estimates based on the thin strip solution. The ideal diamagnetic moment, the saturation moment, the field of full penetration, and the complete magnetization curves are given for all side ratios $0<b/a<\infty$. [S0163-1829(96)01429-4]

I. INTRODUCTION

Magnetzation curves, ac response, flux penetration, and relaxation in superconductors typically are measured with specimens and field orientations that are far from the ideal geometry assumed by existing theories for the evaluation of such experiments. Demagnetizing effects are negligible only in infinitely long, thin slabs or cylinders in a parallel magnetic field. The introduction of a demagnetizing factor accounts for these effects only in the special case of ellipsoids with linear magnetic response. The magnetization curves of superconductors with pinned flux lines, however, are highly nonlinear and hysteretic, and ellipsoidal specimens are difficult to produce. In parallel geometry this nonlinear hysteretic response often is well described by the Bean model[1] and its extensions.[2–5] The Bean model successfully explains also the flux-density profiles observed at the flat end planes of long cylindric or prismatic superconductors but only in the fully penetrated critical state and when corrections for end effects are accounted for.[6]

To obtain maximum signal, magnetization experiments are often performed with thin flat specimens in a perpendicular field, e.g., small monocrystals of high-T_c superconductors or strips with rectangular cross section, see inset in Fig. 1. In this common geometry none of the classical theories of flux penetration applies; only the fully penetrated critical state is well understood provided the Bean assumption of constant critical current density J_c holds. However, if the specimen is much thinner than wide (e.g., a film evaporated on a substrate) one may use recent theories that treat the superconductor as a two-dimensional (2D) medium. These 2D theories consider a circular disk[7–9] or long strip[10–12] with field independent critical current density J_c by extending the original Bean model to this perpendicular geometry, or a strip[13,14] or disk[15] with general linear response, which is observed in the regime of thermally assisted flux flow,[16] see Gilchrist[17] for a short comparative overview. Analytic expressions for the static magnetization and for flux and current profiles are available for the perpendicular Bean model[7–12] of strips and disks and for thin strips with a geometric edge barrier.[18,19] The dynamic response of strips and disks in the linear[13–15] and nonlinear[20,21] cases can be computed by a direct time-integration method, which also works for inhomogeneous superconductors.[22,23]

The one-dimensional (1D) theory of thin long strips and circular disks has recently been extended to the 2D problems of thin superconductors with square or rectangular shape in a

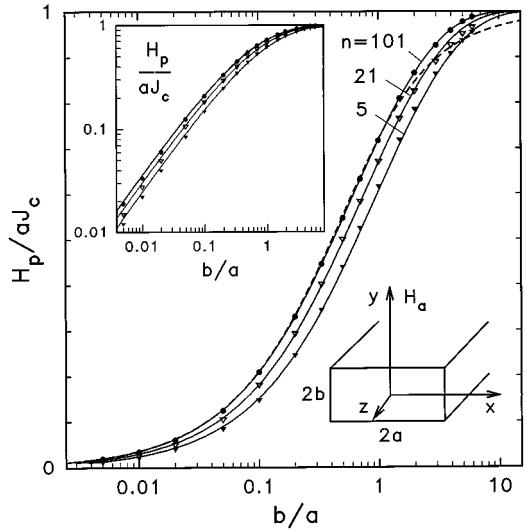

FIG. 1. The field H_p of full penetration of current and flux into a bar of rectangular cross section $2a\times 2b$ in a perpendicular magnetic field, see the lower inset. The material is characterized by a current-voltage law $E(J)=E_c(J/J_c)^n$. Plotted is the H_p computed from Eq. (24) vs the side ratio $0.005\leqslant b/a\leqslant 6$ (symbols) and the fits, Eq. (64), for creep exponents $n=101$ (Bean limit), $n=11$ (weak creep), and $n=5$ (strong creep) (solid lines). The dashed line gives the exact penetration field (65) of the Bean model. The upper inset shows the same data on a log-log plot.

perpendicular field.[23–26] These first-principle's calculations of thin rectangular nonlinear conductors were preceded by numerical inversion methods[27–29] which calculate the sheet current flowing in these squares from the measured profiles of the perpendicular flux density component. Such measurements are possible at the surface of the superconductor by magneto-optics[6,21–23,27] and by Hall probes.[18,28] General expressions for the linear ac susceptibility $\chi(\omega)$ in terms of a sum over first-order poles in the complex ω plane are available for conductors with linear complex ac resistivity in the shape of slabs, cylinders,[30,16] and bars of various cross sections[15] in a parallel field, and for strips,[31] disks,[31,32] and rectangles or squares[24] in perpendicular field. Universal properties of thin superconductors during flux creep in slabs,[33,34] disks and strips[35] and rectangles[25,36] were predicted and observed. The linear ac response during creep in parallel[37] and perpendicular[38] geometries was shown to be independent of the applied field, temperature, and material properties, depending only on the geometry and on the time elapsed since the creep has started (Sec. IV D 3).

Apart from some analytic calculations for ellipsoids (approximate Bean model[4,5] and linear ac response[39,40]) and the computation of the Bean critical state in thick disks,[6,41,42] all the above-quoted theories consider either the parallel limit (infinite thickness) or perpendicular limit (zero thickness), which both assume a current density that does not depend on the coordinate parallel to the homogeneous applied field $\mathbf{B}_a$. Nevertheless, from the 1D theories of thin strips one can draw some conclusions on the current density profile across the thickness, which may form a current-caused longitudinal Bean critical state, and on the shape of the penetrating flux front, cf. Figs. 2 and 3. The exact 2D method given below confirms some of these predictions and outlines their limits.

In the present paper I show how the finite thickness $d=2b$ of realistic specimens can be accounted for by time integration of a relatively simple integral equation to obtain the nonlinear response, flux penetration, creep, etc., or by solving a linear integral equation (or inverting a matrix) to obtain the linear complex and frequency dependent response. The presented method yields detailed profiles of the flux and current densities in the bulk and at the surface. It is based on the observation that, if the specimen is sufficiently long or rotationally symmetric, the general 3D problem, which can be solved only with large numerical effort by little transparent finite-element algorithms, reduces to a 2D problem that can be solved easily on a personal computer. The present paper (part I) introduces the general method and applies it to long strips and slabs of rectangular cross section in a perpendicular field, Fig. 1. Similar results for circular disks and cylinders of arbitrary height in an axial field will be given in a forthcoming part II.[43]

The present 2D electrodynamic problem of bars or thick disks in a perpendicular field should not be confused with the different 2D problem of thin rectangular conductors or superconductors in a perpendicular field. In the thin film geometry the currents are restricted to a plane and have two components, which are connected by $\mathrm{div}\mathbf{J}=0$. The present finite thickness geometry is simpler in a sense, because the current density J, electric field E, and vector potential A have only *one* component, which is directed along the strip or along concentric circles. As one consequence, the contour lines of

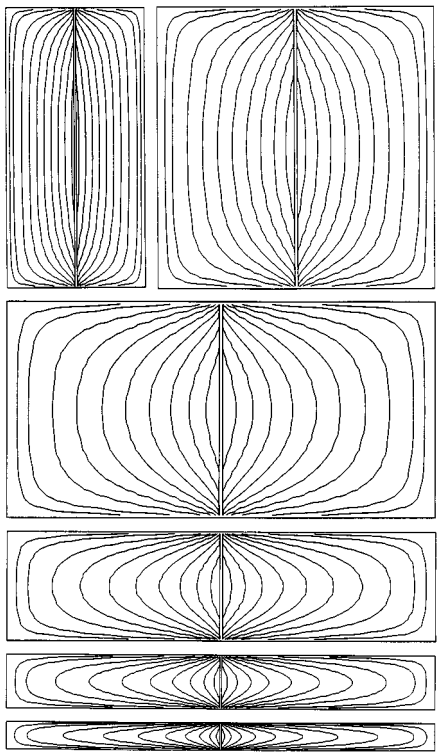

FIG. 2. Current and flux fronts during penetration of a gradually increased perpendicular magnetic field H_a of vertical orientation ($\|y$) into long superconductor bars of side ratios $b/a=2$, 1, 0.5, 0.25, 0.125, 0.0625 (from top to bottom). Shown are the two symmetric contour lines where the current density $J(x,y)\|z$ equals $\pm J_c/2$ for 11 field values $H_a/H_p=0.05$, 0.1, 0.2, . . . , 0.9, 1; H_p is the field of full penetration, Eq. (64), $H_p/J_c a=0.85$, 0.70, 0.51, 0.36, 0.23, and 0.14 . In the depicted Bean limit ($n=21$) one has $J=\pm J_c$ outside, and $J=0$ inside, the two contour lines. Note that above some value of H_a the flux- and current-free central region disconnects from the surface.

A coincide with the magnetic field lines. Furthermore, the time derivative of the scalar A in this geometry gives the electric field E that inserted into the given $E(J)$ law yields the current density $J(E)$ and the magnetization, which is an integral over J. Of course, both 2D problems derive from the same 3D Maxwell equations $\nabla\times\mathbf{H}=\mathbf{J}$ (with the displacement current disregarded) and $\nabla\times\mathbf{E}=-\dot{\mathbf{B}}$. In both cases the reduction to a 2D problem results in a nonlocal relation between the current density and the magnetic field, which leads to an integral equation for the scalar function $J(x,t)$ or $J(r,t)$ in thin strips or disks, or for the density of the current loops $g(x,y,t)$ in thin rectangles, or for $J(x,y,t)$ or $A(x,y,t)$ in the present geometry, see below. All these integral equations contain the appropriate differential equations plus the boundary conditions. They are thus more suitable for numerical calculations since they do not require the computation of spatial derivatives.

As in the previous problems I assume here the material laws $\mathbf{B}=\mu_0\mathbf{H}$, which is a good approximation when everywhere inside the superconductor the flux density B and the critical sheet current $J_c d$ are larger than the lower critical field B_{c1} of the superconductor, and $\mathbf{E}=\rho(J)\mathbf{J}$, which means an, in general, nonlinear but local and isotropic (scalar) re-

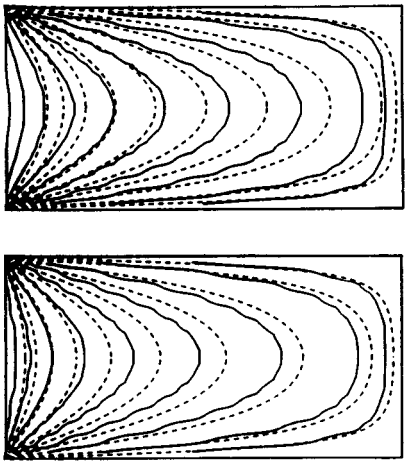

FIG. 3. Comparison of the computed flux fronts (bold) with the estimate (71) (dashed) for strips with $b/a=0.1$ (top) and $b/a=0.05$ (bottom). For clarity in this plot the specimen thickness $d=2b$ is stretched by factors 2.5 (top) and 5 (bottom). The slight wiggle of the computed fronts is due to the small number N_y in the used grid of $N_xN_y=60\times9$ and 70×8 points, and to the large creep exponent $n=21$.

sistivity $\rho(J)=E(J)/J$. For concrete applications to flux penetration or exit and creep, I shall consider the model

$$\mathbf{E}(J)=E_c|J/J_c|^n\mathbf{J}/J=\rho_c|J/J_c|^{n-1}\mathbf{J}, \tag{1}$$

with $1\leqslant n<\infty$. This power law is observed in numerous experiments and was used in theories on creep[35,36,44] and flux penetration[21–23] and ac susceptibility.[23,26,45,46] It corresponds to a logarithmic current dependence of the activation energy $U(J)=U_c\ln(J_c/J)$, which inserted into an Arrhenius law yields $E(J)=E_c\exp(-U/kT)=E_c(J/J_c)^n$ with $n=U_c/kT$. The model (1) contains only two independent parameters E_c/J_c^n and n and interpolates from ohmic behavior ($n=1$) over typical creep behavior ($n=10\cdots20$) to ''hard'' superconductors with Bean behavior ($n\to\infty$).

Extensions of the presented numerical method to anisotropic and even nonlocal resistivity, if required, are straightforward, also the inclusion of the Hall effect. The extension to arbitrary reversible magnetization curve $\mathbf{B}=\mu(H)\mathbf{H}$ is more difficult, but this extension (the consideration of finite B_{c1}) will allow to compute the important geometric edge barriers[47,18,19,26] and the ''current string'' predicted and observed by Indenbom and co-workers[48] in specimens with thickness much larger than the London penetration depth λ. Work in this direction is under way.

In Sec. II the equations of motion for the current density $J(x,y,t)$ are derived for bars with arbitrary and rectangular cross sections in a time dependent perpendicular field. Section III shows how these 2D equations reduce to the known 1D equations for the perpendicular and parallel geometry limits and how the nonlocality arises. Various numerical and analytical solution methods are described and useful general formulas given in Sec. IV. A selection of numerical results for flux penetration and creep is presented in Sec. V.

II. EQUATIONS OF MOTION

A. General bar in a perpendicular field

This section presents a method which calculates the electrodynamics of a conductor or superconductor with general current-voltage characteristics $E(J)$ and arbitrary cross section in the xy plane when a time dependent homogeneous magnetic field $H_a\|y$ is applied. The conductor is assumed to be translational invariant along the direction z perpendicular to H_a (Fig. 1) but the method works also for conductors which possess a rotational axis parallel to H_a.[43] We further assume that no current is fed into the conductor by contacts, but this condition may be relaxed if desired. The applied field induces currents in the bulk and at the surface of the specimen which flow along z. The current density $\mathbf{J}=J(x,y)\hat{\mathbf{z}}$ generates a planar magnetic field $\mathbf{H}$ which has no z component. Since we assume $\mathbf{B}=\mu_0\mathbf{H}$ where $\mathbf{B}=\nabla\times\mathbf{A}$ is the induction and $\mathbf{A}=A(x,y)\hat{\mathbf{z}}$ the vector potential, we may write $\mathbf{J}=\nabla\times\mathbf{H}=\mu_0^{-1}\nabla\times(\nabla\times\mathbf{A})=-\mu_0^{-1}\nabla^2\mathbf{A}$, thus the scalar fields $J(x,y)$ and $A(x,y)$ obey the 2D Laplace equation $\mu_0J=-\nabla^2A$. Since we are interested only in the current density J inside the specimen, the vector potential in this equation should be interpreted as the part A_J of $A=A_a+A_J$ which is generated by this current, while the remaining part $A_a=-xB_a$ is generated by the current in the coil that produces the applied field $B_a=\mu_0H_a$. However, since $\nabla\times\mathbf{A}_a=B_a\hat{\mathbf{z}}$ is constant inside the specimen, one has $\nabla^2A_a=0$ there, and thus one may write both $\mu_0J=-\nabla^2A$ or $\mu_0J=-\nabla^2(A-A_a)=\nabla^2A_J$. This means that the applied field drops out from the differential equations for A and J and thus has to be considered separately by appropriate boundary conditions for $\mathbf{H}$, requiring the calculation of $\mathbf{H}$ in the entire space.

The computation can be simplified drastically if one finds an equation of motion for the current density $J(x,y,t)$ *inside the conductor alone*, which should contain the time dependent applied field $B_a(t)$ explicitly as an external driving force that generates a non-zero solution. Such equations of motion were derived for strips,[13] disks,[15] and rectangles[24] in perpendicular field, and for a slab in parallel field,[49] see also Sec. III B. To obtain such an equation for the present geometry, we proceed as follows. First we write down the general solution to the 2D Laplace equation $\mu_0J=-\nabla^2(A+xB_a)$,

$$A(\mathbf{r})=-\mu_0\int_S d^2r'\,Q(\mathbf{r},\mathbf{r}')J(\mathbf{r}')-xB_a \tag{2}$$

with $\mathbf{r}=(x,y)$ and $\mathbf{r}'=(x',y')$ and the integral kernel

$$Q(\mathbf{r},\mathbf{r}')=\frac{\ln|\mathbf{r}-\mathbf{r}'|}{2\pi}. \tag{3}$$

The integration in (2) is over the cross section S of the specimen, the area to which the current density J is confined. Formally, Eq. (2) may be inverted and written in the form

$$J(\mathbf{r})=-\mu_0^{-1}\int_S d^2r'\,Q^{-1}(\mathbf{r},\mathbf{r}')[A(\mathbf{r}')+x'B_a]. \tag{4}$$

Here $Q^{-1}(\mathbf{r},\mathbf{r}')$ is the inverse kernel defined by

$$\int_S d^2r' Q^{-1}(\mathbf{r},\mathbf{r}')Q(\mathbf{r}',\mathbf{r}'') = \delta(\mathbf{r}-\mathbf{r}''). \tag{5}$$

The kernel (3) satisfies $\nabla^2 Q(\mathbf{r}-\mathbf{r}') = \delta(\mathbf{r}-\mathbf{r}')$. Therefore, in the infinite space the application of $\int Q^{-1}$ would be identical to the application of the Laplacian operator $\nabla^2 = \partial^2/\partial x^2 + \partial^2/\partial y^2$. However, since the integrals in (2) and (4) are confined to the specimen cross section, Q^{-1} is different from ∇^2 and contains information about the specimen shape. One can show that the first term in the integral (4) yields the *bulk current* while the second term is the *surface screening current* that exactly compensates the applied field inside the specimen. This surface current plays the role of the H_a-dependent boundary condition in an equation for J. The inverse kernel may be computed by inverting a matrix as shown in Sec. IV A.

Next we express the induction law $\nabla\times\mathbf{E} = -\dot{\mathbf{B}} = -\nabla\times\dot{\mathbf{A}}$ in the form $E = -\dot{A}$. The arbitrariness of the gauge of $\mathbf{A}$, to which an arbitrary curl-free vector field may be added, presents no problem in this simple geometry. With the material law $E = E(J)$, e.g., $E = E_c(J/J_c)^n \mathrm{sgn}(J)$ (1) or a general linear and complex $E = \rho J$, one gets $\dot{A} = -E(J)$. This relation between $\dot{A}$ and J allows one to eliminate from Eq. (2) either A or J. Eliminating A, one obtains an equation of motion for $J(x,y,t)$,

$$E[J(\mathbf{r},\mathbf{t})] = \mu_0 \int_S d^2r' Q(\mathbf{r},\mathbf{r}')\dot{J}(\mathbf{r}',t) + x\dot{B}_a(t). \tag{6}$$

This implicit equation for the current density $J(\mathbf{r},t)$ contains the time derivative $\dot{J}$ under the integral sign. It may be used in this form (containing the kernel Q rather than Q^{-1}) if one is interested in the linear response to a periodic signal $\dot{B}_a \propto i\omega\exp(i\omega t)$. In this case the time dependence of $\dot{J}(\mathbf{r},t) = J(\mathbf{r})\exp(i\omega t)$ is explicitly known and the amplitude $J(\mathbf{r})$ follows from a linear integral equation[13–15,31,38] (Sec. IV D). In the special case of flux creep, i.e., when B_a is held constant and thus $\dot{B}_a = 0$, Eq. (6) can be solved analytically by separation of the variables in $E(\mathbf{r},t) = f(\mathbf{r})g(t)$ (Sec. IV B). This separation works if $E(J)$ is sufficiently nonlinear[33–35] or if the power law (1) applies.[49] Equation (6) for $J(\mathbf{r},t)$ may be written as an equation for $E(\mathbf{r},t)$ by noting that $\dot{J} = \dot{E}(\partial J/\partial E)$ where $\partial J/\partial E = 1/E'(J)$ is the given differential conductvity. A further problem where the separation of variables works is given in Sec. IV C.

In the general case of nonlinear $E(J)$ and arbitrary sweep of $B_a(t)$, the time integration of (6) has to be performed numerically as described in Sec. IV A. For this purpose, the time derivative should be moved out from the integral to obtain $\dot{J}$ as an explicit functional of J and $\dot{B}_a$. This inversion is achieved by using Eq. (4) instead of Eq. (2). The equation of motion for $J(\mathbf{r},t)$ then reads

$$\dot{J}(\mathbf{r},t) = \mu_0^{-1} \int_S d^2r' Q^{-1}(\mathbf{r},\mathbf{r}')\{E[J(\mathbf{r}',t)] - x'\dot{B}_a(t)\}. \tag{7}$$

This integral equation is easily time integrated by starting with $J(\mathbf{r},0) = 0$ at time $t = 0$ and then putting, $J(\mathbf{r},t+dt) = J(\mathbf{r},t) + \dot{J}(\mathbf{r},t)dt$.

Note that Eq. (7) does not contain the applied field $B_a(t)$ itself but only its time derivative, the ramp rate $\dot{B}_a(t)$. This property applies also to the corresponding equations of motion of the previously treated perpendicular geometry of strips,[13] disks,[15] and rectangles.[24–26] Remarkably, in the present perpendicular bar geometry, one can also find an equation of motion which contains the field $B_a(t)$ itself. Namely, by inserting the relation $J\{A\}$, Eq. (4), into the induction law $\dot{A} = -E(J)$ using a given $E(J)$ model, one obtains an equation for the vector potential $A(\mathbf{r},t)$ alone,

$$\dot{A}(\mathbf{r},t) = -E[J(\mathbf{r},t)],$$

$$J(\mathbf{r},t) = -\mu_0^{-1} \int_S d^2r' Q^{-1}(\mathbf{r},\mathbf{r}')[A(\mathbf{r}',t) + x' B_a(t)]. \tag{8}$$

Both Eqs. (7) and (8) work equally well when incorporated into numerical programs as described in Sec. IV A.

Equations describing superconductors in the Meissner state with London penetration depth λ are obtained by inserting in (2), (4), or (8) $A = -\mu_0\lambda^2 J$, and in (6) or (7) $E = \mu_0\lambda^2\dot{J}$. The time dependence of the resulting linear equation for J or E separates; it thus suffices to solve it for one value of B_a or $\dot{B}_a$ as described in Sec. IV C 4.

B. Strips and bars with rectangular cross section

In typical experiments the superconductor samples have rectangular cross section with B_a applied along one of the symmetry axes x or y. In this particular case, or more generally if the specimen exhibits two mirror planes $x = 0$ and $y = 0$, the integrations in the above expressions may be restricted to one-quarter of the specimen cross section $-a \leqslant x \leqslant a$, $-b \leqslant y \leqslant b$, e.g., to $0 \leqslant x \leqslant a$, $0 \leqslant y \leqslant b$. One then has to use a symmetric kernel Q_{sym}, which follows from the symmetry of the current density J. When B_a is along y, then J, E, and A are odd functions of x and even functions of y, e.g., $J(x,y) = -J(-x,y) = J(x,-y)$. The symmetric kernel $Q_{\mathrm{sym}} = Q(x',y') - Q(-x',y') + Q(x',-y') - Q(-x',-y')$ with Q from (3) may be written in the compact form

$$Q_{\mathrm{sym}}(\mathbf{r},\mathbf{r}') = \frac{1}{4\pi}\ln\frac{(x_-^2+y_-^2)(x_-^2+y_+^2)}{(x_+^2+y_-^2)(x_+^2+y_+^2)} \tag{9}$$

with $x_\pm = x \pm x'$, $y_\pm = y \pm y'$. For example, Eq. (2) now reads for the rectangular cross section

$$A(\mathbf{r}) = -\mu_0 \int_0^a dx' \int_0^b dy' Q_{\mathrm{sym}}(\mathbf{r},\mathbf{r}')J(\mathbf{r}') - xB_a\,. \tag{10}$$

Defining the inverse kernel Q_{sym}^{-1} of (9) we may write the equation of motion (7) in the form

$$\dot{J}(\mathbf{r},t) = \mu_0^{-1} \int_0^a dx' \int_0^b dy' Q_{\mathrm{sym}}^{-1}(\mathbf{r},\mathbf{r}')[E(J) - x'\dot{B}_a]. \tag{11}$$

With appropriately modified boundary $b = b(x)$, Eqs. (10) and (11) apply also to specimens with varying thickness $2b(x)$ as long as these still possess the mirror planes $x = 0$

and $y=0$. For example, to describe a circular cylinder with radius a in a perpendicular field, one just replaces the integration boundary b in the integral over y by the function $b(x)=(a^2-x^2)^{1/2}$. The inverse kernel $Q_{\rm sym}^{-1}$ defined by Eq. (5) depends on the specimen shape and thus also on $b(x)$.

C. Disks and cylinders in an axial field

For completeness I give here also the equation for conductors with a rotational axis parallel to B_a and with maximum radius a. The height $2b$ is constant for disks ($b \ll a$) and long cylinders ($b \gg a$), but in general $b(r)$ may be an arbitrary function of the radius $r=(x^2+z^2)^{1/2}$, e.g., $b(r)=(a^2-r^2)^{1/2}$ for spheres and $b(r)=b(0)(1-r^2/a^2)^{1/2}$ for rotational ellipsoids. In this cylindrical geometry the current density, electric field, and vector potential have only *one* component, which points along the azimuthal direction $\hat{\varphi}$, thus $\mathbf{J}=J(r,y)\hat{\varphi}$, $\mathbf{E}=E(r,y)\hat{\varphi}$, and $\mathbf{A}=A(r,y)\hat{\varphi}$. The vector potential of the applied field $\mathbf{B}_a=B_a\hat{\mathbf{y}}$ is $A_a=-(r/2)B_a$. The solution of the Laplace equation $\mu_0 J=-\nabla^2[A_J+(r/2)B_a]$ reads in this cylindrical geometry

$$A(\mathbf{r})=-\mu_0\int_0^a dr'\int_0^b dy'\,Q_{\rm cyl}(\mathbf{r},\mathbf{r}')J(\mathbf{r}')-\frac{r}{2}B_a, \tag{12}$$

where now $\mathbf{r}=(r,y)$ and $\mathbf{r}'=(r',y')$ and the kernel is

$$Q_{\rm cyl}(\mathbf{r},\mathbf{r}')=f(r,r',y-y')+f(r,r',y+y'),$$

$$f(r,r',\eta)=\int_0^\pi \frac{d\varphi}{2\pi}\frac{r'\cos\varphi}{(\eta^2+r^2+r'^2+2rr'\cos\varphi)^{1/2}}. \tag{13}$$

This kernel was obtained by integrating the 3D Green function of the Laplace equation, $1/(4\pi|\mathbf{r}_3-\mathbf{r}'_3|)$ with $\mathbf{r}_3=(x,y,z)$, over the angle $\varphi=\arctan(z/x)$, while the kernel (3) was obtained by integrating $1/(4\pi|\mathbf{r}_3-\mathbf{r}'_3|)$ over z from $-\infty$ to ∞. If desired, the integral kernel (13) may be expressed in terms of elliptic integrals, but for computational purposes it is more convenient to evaluate the φ integral (13) numerically.

The equation of motion for the azimuthal current density $J(r,y,t)$ is obtained in the same way as Eqs. (7) and (11), yielding

$$\dot{J}(\mathbf{r},t)=\mu_0^{-1}\int_0^a dr'\int_0^b dy'\,Q_{\rm cyl}^{-1}(\mathbf{r},\mathbf{r}')\left(E(J)-\frac{r'}{2}\dot{B}_a\right). \tag{14}$$

Note the similarity of (14) with the corresponding equation (11) for the current density in strips, bars, or slabs. Therefore, the same numerical program can be used to compute the electrodynamics for long bars in perpendicular field and for rotationally symmetric specimens in axial field. One just has to replace in (11) the integral kernel $Q_{\rm sym}$ (9) by $Q_{\rm rot}$ (13), multiply B_a by a factor 1/2, and interpret the coordinate x as the radius r. Note that these equations describe also cylinders in both perpendicular and parallel fields.

III. PERPENDICULAR AND PARALLEL LIMITS

Formulas (9)–(11) for bars with rectangular cross section $2a\times 2b$ in a perpendicular field allow one to see how the limits of thin conductors in (a) parallel and (b) perpendicular fields are reached. In these two limiting geometries, linear and nonlinear conductors or superconductors show quite different behavior. For example, in the Bean model $|J|\leqslant J_c$, they exhibit qualitatively different current and field profiles during penetration of flux: (a) Constant current density $J=0$ or $J=\pm J_c$ and constant slope of $B(x)$;[1] (b) a flux front with vertical slopes of J and B, and a logarithmic infinity of B at the edges.[11] The Bean magnetization curves $M(H_a)$ during flux penetration are also different in these two geometries: (a) an inverted parabola with constant M for $H_a \geqslant J_c a$; (b) a hyperbolic tangent which in the limit of zero thickness does not saturate, cf. Sec. V F. The parallel results are easily derived since demagnetizing effects are absent and the problem is one dimensional; they follow directly from Bean's assumption $|J|\leqslant J_c$ or, when $E=\rho J$ is linear, from the linear diffusion equation for $B(x,t)$ or $J(x,t)$ with flux diffusivity $D=\rho/\mu_0$. The perpendicular results were obtained from a static or dynamic integral equation for the sheet current in Refs. 7–15.

I show now how all these results for strips and slabs follow naturally from Eq. (11). A similar derivation of the limiting cases of thin circular disks or long cylinders from Eq. (14) will be given elsewhere.[43]

A. Perpendicular limit $b \ll a$

If the thickness $d=2b$ of a strip is much smaller than its width $2a$, the integral kernel (9) varies little over the thickness and may be replaced by its value in the plane $y=0$. This means that only the current density integrated over the thickness enters the static equation (10), the sheet current, or line current

$$J_s(x)=\int_{-b}^b J(x,y)dy. \tag{15}$$

Therefore, the equations for the statics of thin strips contain only the sheet current $J_s(x)$; the local current density $J(x,y)$ is required only if one wants to know the parallel field component $B_x(x,y)=-\int_0^y J(x,y)dy$ *inside* the strip, which determines also the local slope B_y/B_x of the curved vortices in the strip.[50] The perpendicular component $B_y(x,y)\approx B_y(x,0)$ and the magnetic field at and near the surface of the strip, however, depend only on $J_s(x)$ (15). Only this sheet current and the critical sheet current $J_{sc}=J_c d$ enter the perpendicular Bean models,[7–12] irrespective of how the currents are distributed across the thickness. One may have, e.g., $J(x,y)=\text{const}$, or $J(x,y)\propto\cosh(y/\lambda)$ where λ is the London penetration depth, or $J(x,y)=0$ in a central layer $|y|<y_0$ and $J(x,y)=\pm J_c$ in two surface layers $|y|\geqslant y_0$ (a current caused Bean state across the thickness). The equations for $J_s(x)$ even allow for a varying thickness $2b(x)$ and for a space dependent $J_{sc}(x)$.

From the implicit equation of motion (6) one might argue that for thin strips the dynamics, too, depends only on the integrated current $J_s(x)$ (15). However, the inverted and explicit equation of motion (7) and its symmetric version (11) show that even when $Q_{\rm sym}$ does not depend on y and y' since $b \ll a$ is small, the y dependence of $J(x,y)$ has to be known because the integration in (11) is over E rather than

J. Only when $E(J)$ is linear does the sheet current J_s (15) uniquely determine the average $\int_{-b}^{b} E(x,y)dy$. Therefore, for general nonlinear $E(J)$ the 2D dynamic equation (11) reduces to a 1D equation only if $J(x,y)$ does not depend on y. In this case one has $J_s = Jd$. The general 2D equation (11), however, remains valid for arbitrarily inhomogeneous $J(x,y)$, also for nonlinear $E(J)$, and even for inhomogeneous materials or B dependent $J_c(B)$.

With the above restrictions in mind, one may express Eqs. (6) and (11) as equations of motion for the sheet current $J_s(x,t)$ in a strip in perpendicular field $B_a(t)$,

$$E\left[\frac{J_s(x,t)}{d}\right] = \mu_0 \int_0^a dx' Q_{\rm tra}(x,x') \dot{J}_s(x',t) + x\dot{B}_a, \quad (16)$$

$$\dot{J}_s(x,t) = \mu_0^{-1} \int_0^a dx' Q_{\rm tra}^{-1}(x,x') \left[E\left(\frac{J_s}{d}\right) - x'\dot{B}_a \right], \quad (17)$$

where the 1D transverse kernel is $Q_{\rm sym}$ at $y = y' = 0$,

$$Q_{\rm tra}(x,x') = Q_{\rm sym}(x,0,x',0) = \frac{1}{2\pi} \ln \left| \frac{x-x'}{x+x'} \right| \quad (18)$$

and $Q_{\rm tra}^{-1}(x,x')$ is its inverse. These equations were used in Refs. 13–15 and 20–22 to derive the dynamic and quasistatic behavior of thin superconductor strips in a perpendicular field.

B. Parallel limit $b \gg a$

When the thickness of the strip is increased more and more until $b \gg a$, one arrives at the longitudinal limit of a slab in parallel field. In this limit $J(x,y,t)$ becomes independent of y if one disregards the deviating behavior near the far-away edges $y = \pm b$. The 2D integral equations (6) and (11) for $J(x,y,t)$ then reduce to 1D equations as in the perpendicular limit, but now for the current density $J(x,t)$ rather than for the sheet current $J_s(x,t)$. These 1D equations are thus as general as Eqs. (6) and (11) and describe both the static and dynamic behavior of the slab. Defining $J(x,t) = J(x,0,t)$, one may write these 1D equations of motion in the form

$$E[J(x,t)] = \mu_0 \int_0^a dx' Q_{\rm long}(x,x') \dot{J}(x',t) + x\dot{B}_a, \quad (19)$$

$$\dot{J}(x,t) = \mu_0^{-1} \int_0^a dx' Q_{\rm long}^{-1}(x,x') [E(J) - x'\dot{B}_a], \quad (20)$$

with the 1D longitudinal kernel $(x,x' \geq 0)$

$$Q_{\rm long}(x,x') = \int_0^\infty Q_{\rm sym}(x,0,x',y')dy' = \frac{1}{2}(|x-x'| - |x+x'|)$$

$$= -\min(x,x'), \quad (21)$$

i.e., one has $Q_{\rm long} = -x$ for $0 < x < x'$ and $Q_{\rm long} = -x'$ for $0 < x' < x$. To derive (21) I have used the formula[51]

$$\int_0^\infty \ln \frac{p^2+y^2}{q^2+y^2} dy = \pi(p-q). \quad (22)$$

The kernel (21) has the property $\partial^2 Q_{\rm long}(x,x')/\partial x^2 = \delta(x-x')$. Therefore, by taking the second derivatives on both sides of Eq. (19) one arrives at a differential equation for the electric field

$$E''(x) = \mu_0 \dot{J}(x,t) = \mu_0 \frac{\partial J}{\partial E} \dot{E}(x,t). \quad (23)$$

This diffusion equation with diffusivity $D = \mu_0^{-1} \partial E/\partial J$ could have been obtained directly from the above Maxwell equations $\mu_0 J = -\nabla^2 A$ and $E = -\dot{A}$. However, the applied field has now dropped out by taking the second derivative. Therefore, for practical calculations the integral equation (19) and its inverse (20) are more suited than differential equations of the type (23) because they incorporate the boundary conditions for B or A, $B(x = \pm a,t) = -A'(x = \pm a,t) = B_a(t)$ in an equation for the current density $J(x,t)$.

C. Local and nonlocal diffusion

From the differential equation (23) one can see that the equivalent integral equation (20) describes the diffusion of the electric field $E(x,t)$ or current density $J(x,t)$ under a driving force given by $\dot{B}_a$ and with the boundary conditions contained in the integral kernel $Q_{\rm long}^{-1}$ and in the integration boundaries. This diffusion in general is *nonlinear* when the $E(J)$ law is not linear. In the parallel geometry the diffusion is *local*, since in Eq. (23) $\dot{E}(x,t)$ depends only on $E''(x,t)$ at the same position x. In contrast to this, in the perpendicular geometry the diffusion is *nonlocal* since Eq. (17) cannot be written as a differential equation for the sheet current $J_s(x,t)$. Of course, the original 3D Maxwell equations used here are local. The nonlocality is an artifact coming from the reduction of the dimensionality to obtain an equation of motion for the 2D sheet current. One may say that each point in the thin conductor interacts with all other points via the magnetic stray field in the outer space.

The question whether our general equations of motion for $J(x,y,t)$ or $A(x,y,t)$ in a bar or thick disk describe local or nonlocal diffusion is less clear. The general Eqs. (6)–(8) for bars of arbitrary cross section may be called local diffusion equations since they can be expressed as differential equations with appropriate boundary conditions. Equations (11) and (14) for the rectangular bar or for the circular disk describe the same local diffusion, but now the imposed symmetry formally causes an interaction of each point (x,y) with itself and with its image points $(-x,y)$, $(x,-y)$, and $(-x,-y)$ in the rectangle, or with all points on a circle in the disk, via the symmetric integral kernels $Q_{\rm sym}$ (9) or $Q_{\rm disk}$ (13). So, one may say that imposing boundary or symmetry conditions formally introduces some nonlocality in otherwise local diffusion problems. This nonlocality becomes visible from the compact formulation of such a problem in terms of an integral equation. But not in all cases can an integral equation be transcribed into a differential equation, e.g., the integral equations (16) and (17) for the 2D sheet current.

IV. SOLUTION METHODS

A. Flux penetration: Time integration

To obtain the current and field profiles and the magnetization during penetration of perpendicular flux into long bars with nonlinear $E(J)$ law, one has to integrate Eq. (11) numerically. This may be done easily on a personal computer by tabulating the functions J, E, and A on a 2D grid with equidistant points $x_k=(k-1/2)a/N_x$ $(k=1,2,\ldots,N_x)$ and $y_l=(l-1/2)b/N_y$ $(l=1,2,\ldots,N_y)$, choosing $N_y\approx bN_x$ and the length unit $a=1$. Labeling the points (x_k,y_l) by one index $i=1,2,\ldots,N$ with $N=N_xN_y$, the functions $J(x,y,t)$, etc., become time dependent vectors $J_i(t)$ with N components, and the integral kernel $Q_{\rm sym}$ (9) becomes an $N\times N$ matrix Q_{ij}. The inverse kernel $Q_{\rm sym}^{-1}$ also becomes a $N\times N$ matrix, Q_{ij}^{-1}, which is obtained by inverting the matrix Q_{ij}. One has $\Sigma_l Q_{il}Q_{lj}^{-1}=\delta_{ij}$ where $\delta_{ij}=1$ if $i=j$ and $\delta_{ij}=0$ else. The calculation and inversion of the matrix Q_{ij} has to be performed only once at the beginning of the computation.

With the power law (1) and in reduced units $\mu_0=a=J_c=E_c=1$, yielding $E=J^n$, the equation of motion (11) takes the form

$$\dot J_i(t)=\frac{b}{N}\sum_j Q_{ij}^{-1}[J_j(t)^n-x_j\dot B_a(t)]. \tag{24}$$

The time integration of this system of nonlinear differential equations of first order for the $J_i(t)$ is straightforward. One may start with $J_i(0)=0$ and then increase the time in steps dt, putting $J_i(t+dt)=\dot J_i(t)dt$. More elaborate methods are conceivable, also with nonequidistant grids as described in Refs. 13 and 15, but for our bar geometry this simple method is very stable and fast and yields beautiful pictures of flux penetration (Sec. V). An important hint is, however, that at each time the time step should be chosen inversely proportional to the maximum value of the resistivity $\rho_i=E_i/J_i=|J_i|^{n-1}$, e.g., $dt=c_1/[\max\rho_i(t)+c_2]$ with $c_1=0.3/(N_x^2n)$ and $c_2=0.01$. This choice provides optimum computational stability and speed. The computation time is thus proportional to $N^2/dt\propto N_x^4N_y^2n$.

From the computed current density $J(x,y,t)$ the magnetization is obtained by integration (or summation of the x_iJ_i) as described in Sec. V F. The vector potential inside the bar may be obtained from the electric field $E=J^n$ by time integration, $A_i(t)=-\int_0^t J_i(t)^n dt$. Alternatively, one may compute $A(x,y,t)$ from the integral (10). This second method yields the vector potential also *outside* the specimen, if the kernel $Q_{\rm sym}$ (9) is also computed for these outer points (x,y). From $A(x,y,t)$ the magnetic field lines are easily plotted noting that they coincide with the contour lines of A. If desired, the field components B_x and B_y, e.g., at the specimen surface, may be calculated as spatial derivatives of A.

A big advantage of the present method is that neither the induction **B** nor any spatial derivative have to be computed in order to obtain the current profiles and magnetization curves during flux penetration or exit. The method thus achieves high accuracy with modest computational effort. Even a grid of only $N=10\times10$ points may be used, see Sec. V. To reach this accuracy the diagonal terms of the matrix $Q_{ij}=Q_{\rm sym}(\mathbf{r}_i,\mathbf{r}_j)$ have to be chosen appropriately. Note that Q_{ij} diverges as $\ln|\mathbf{r}_i-\mathbf{r}_j|$ when $\mathbf{r}_i$ approaches $\mathbf{r}_j$. The optimum choice of the diagonal terms Q_{ii} for this and similar integral kernels may be obtained from a sum rule[13–15] or by expressing the kernel as a finite Fourier series with as many terms as points $\mathbf{r}_i$.[23–25] Recently Gilchrist and Brandt[52] discussed this cutoff problem in some detail for films with circular current flow and show that it is related to the well-known fact that the mutual inductance of two loops is nearly independent of the width or radius of the conductors, but the self-inductances diverge logarithmically when the strip width or wire radius goes to zero. The matrix elements Q_{ij} in our theory may be interpreted as mutual $(i\neq j)$ and self- $(i=j)$ inductances of double strips or loops. For practical purposes it suffices to state that good accuracy is achieved by replacing in the matrix Q_{ij} the terms $\ln|\mathbf{r}_i-\mathbf{r}_j|$ by $(1/2)\ln[(\mathbf{r}_i-\mathbf{r}_j)^2+\epsilon^2]$ where $\epsilon^2=0.015dxdy$ if $dx=a/N_x\approx dy=b/N_y$.

B. Creep: Separation of variables

In at least two special cases the nonlinear nonlocal diffusion equation (6) can be solved analytically by separation of the time and space variables as realized first for the problem of flux creep by Gurevich.[34,35] To see this we write Eq. (6) as an equation for the electric field $E(\mathbf{r},t)$ noting that $\dot J=\dot E/(\partial E/\partial J)$. For the power law $E(J)=E_c(J/J_c)^n$ one explicitly has $\partial E/\partial J=(nE/J_c)(E_c/E)^{1/n}$, yielding[35,49]

$$E(\mathbf{r},t)=\frac{\mu_0J_c}{nE_c^{1/n}}\int d^2r'\,Q(\mathbf{r},\mathbf{r}')\frac{\dot E(\mathbf{r}',t)}{E(\mathbf{r}',t)^{1-1/n}}+x\dot B_a. \tag{25}$$

If B_a is held constant, $\dot B_a=0$, one has the situation of flux creep. In this case an exact solution of Eq. (25) is the ansatz $E=f(\mathbf{r})g(t)$, which gives[49]

$$E(\mathbf{r},t)=E_cf_n(\mathbf{r})\left(\frac{\tau}{t_1+t}\right)^{n/(n-1)}. \tag{26}$$

If we chose $\tau=\mu_0J_cS'/[4\pi(n-1)E_c]$ with S' denoting some arbitrary area, e.g., the specimen cross section S, we obtain $f_n(\mathbf{r})$ from the implicit equation

$$f_n(\mathbf{r})=-\frac{4\pi}{S'}\int_S d^2r'\,Q(\mathbf{r},\mathbf{r}')f_n(\mathbf{r}')^{1/n}. \tag{27}$$

This nonlinear integral equation is easily solved by iterating the relation $f_n^{(m+1)}=-(4\pi/S')\int Qf_n^{(m)1/n}$ starting with $f_n^{(0)}=1$. The resulting series $f_n^{(1)}$, $f_n^{(2)}$, ..., converges rapidly if $n>1$. For $m\gg1$ one has approximately $f_n^{(m+1)}(\mathbf{r})\approx f_n^{(m)}(\mathbf{r})\cdot(1+c/n^m)$ with $c\approx1$. For $n\gg1$ (practically for $n\geq5$) the shape $f_n(\mathbf{r})$ of the electric field becomes a universal function which depends only on the specimen shape but not on the exponent n,

$$f_{n\geq5}(\mathbf{r})\approx f_\infty(\mathbf{r})=-\frac{2}{S'}\int_S d^2r'\ln|\mathbf{r}-\mathbf{r}'|. \tag{28}$$

In the ohmic case $n=1$, the ansatz (26) makes no sense since the exponent $n/(n-1)$ diverges. For this special case the integral equation (25) is linear since the factor

$\partial J/\partial E=\sigma=1/\rho$ is the constant ohmic conductivity. This linear integral equation is solved by the ansatz

$$E(\mathbf{r},t)=E_0 f_1(\mathbf{r})\exp(-t/\tau_1), \tag{29}$$

with $E_0=$const and the relaxation time $\tau_1=\mu_0\sigma S'/\Lambda_1$, where Λ_1 and $f_1(\mathbf{r})$ are the lowest eigenvalue and eigenfunction of the linear integral equation

$$f_\nu(\mathbf{r})=-\Lambda_\nu\frac{2}{S'}\int_S d^2r'\ln|\mathbf{r}-\mathbf{r}'|f_\nu(\mathbf{r}'). \tag{30}$$

In (30) the index $\nu=1,2,\ldots$ labels the eigenvalues and eigenfunctions, which will be required also in Sec. IV D; ν should not be confused with the exponent n, which in general may be any real number $n\geqslant 1$; in this section accidentally $f_n(x,y)$ and $f_\nu(x,y)$ for $n=1$ and $\nu=1$ denote the same function.

From (1) and (26) the current density becomes

$$J(\mathbf{r},t)=J_c|f_n(\mathbf{r})|^{1/n}\left(\frac{\tau}{t_1+t}\right)^{1/(n-1)}\operatorname{sgn}f_n(\mathbf{r}). \tag{31}$$

For large $n\gg 1$ and $t\gg t_1$ the time factor in (31) equals $(\tau/t)^{1/(n-1)}\approx 1-[1/(n-1)]\ln(t/\tau)$ and the spatial factor is $|f_n(\mathbf{r})|^{1/n}\approx 1$. One thus has everywhere $|J|\approx J_c$ with slight creep corrections.

These results still apply to arbitrary shape of the specimen cross section S. For rectangular cross section $S=2a\times 2b$ one may replace in (25) and (27) Q by $Q_{\rm sym}$ (9) and restrict the integration to $0\leqslant x'\leqslant a$, $0\leqslant y'\leqslant b$. In the perpendicular limit $b\ll a$ using $S'=S=4ab$ we get

$$\tau=\mu_0 J_c ab/[\pi(n-1)E_c], \tag{32}$$

$$f_n(x)=\frac{1}{a}\int_0^a dx'\ln\left|\frac{x+x'}{x-x'}\right|f_n(x')^{1/n}, \tag{33}$$

and $E(x,t)\approx E_c f_n(x)(\tau/t)^{n/(n-1)}$. For large creep exponent $n\gg 1$ this reproduces the universal creeping $E(x,t)$ for thin strips of Ref. 35,

$$E(x,t)=\frac{\mu_0 J_c ab}{\pi(n-1)}\frac{1}{t}\left(\ln\frac{a+x}{a-x}+\frac{x}{a}\ln\frac{a^2-x^2}{x^2}\right). \tag{34}$$

Note that the final result $E(x,t)$ (34) is independent of the choice of S'. But the simplicity of Eq. (33) suggests that $S'=4ab$ is the natural choice in the perpendicular limit. In the parallel limit $b\gg a$, the natural choice appears to be $S'=16a^2/\pi$, which yields with (21)

$$\tau=\mu_0 J_c 4a^2/[\pi^2(n-1)E_c], \tag{35}$$

$$f_n(x)=\frac{\pi^2}{4a^2}\int_0^a dx'\min(x,x')f_n(x')^{1/n} \tag{36}$$

for $0\leqslant x\leqslant a$, with $f_n(-x)=-f_n(x)$. The integral equation (35) is equivalent to a differential equation with boundary conditions,

$$f_n''(x)=-k_1^2 f_n(x)^{1/n},\quad f_n(0)=f_n'(a)=0\,, \tag{37}$$

with $k_1=\pi/2a$. The solutions of (37) in the ohmic ($n=1$) and Bean ($n=\infty$) limits look very similar, $f_1(x)=\text{const}\times\sin(\pi x/2a)$ and $f_\infty(x)=(\pi^2/8a^2)x(2a-|x|)$. For large exponents $n\gg 1$ this reproduces the universal creeping electric field

$$E(x,t)=\frac{\mu_0 J_c}{n-1}\frac{x(2a-|x|)}{2t} \tag{38}$$

obtained for slabs in parallel field by Gurevich and Küpfer.[33] The corresponding $E(r,t)$ for long cylinders in parallel field is[25]

$$E(r,t)=\frac{\mu_0 J_c}{(n-1)t}\left[\frac{(3a^2-r_0^2)\ln(r/r_0)}{4[\ln(a/r_0)+1]}-\frac{r^2-r_0^2}{4}\right], \tag{39}$$

where $r_0\ll a$ is an inner cutoff radius, $E(r_0,t)=0$.

For rectangular bars with arbitrary side ratio $0<b/a<\infty$ a useful interpolation is $S'=4ab/(1+\pi b/4a)$. With this choice of S' the iteration of Eq. (27) converges rapidly, and in both limits $b\ll a$ and $b\gg a$, $f_n(x)$ becomes independent of a and b if a is chosen as length unit.[49]

C. Reaching magnetic saturation

The second special case where separation of variables works is when the ramp rate $\dot B_a$ is kept constant until full magnetic saturation is reached. In the Bean limit $n\to\infty$, this saturation occurs when the applied field B_a has reached the field of full penetration B_p, which is computed in Sec. V A as a function of the side ratio b/a. But for finite creep exponent $n<\infty$ the saturation is reached only gradually. I will show now that the approach of saturation is exponential in time.

In the fully saturated state the current density $J(x,y,t)$ does not change any more, and also the electric field $E(x,y,t)$ generated by this current according to the material law $E=E(J)$ (1). The stationary value $E(x,y,\infty)$ is determined by the ramp rate and by the specimen shape as discussed in detail in Ref. 25. For our bar in perpendicular field one has $E(x,y,\infty)=-\dot A_a=x\dot B_a$ as is obvious from Eq. (25). Writing near the saturation $E(x,y,t)=x\dot B_a+E_1(x,y,t)$ we may obtain the small perturbation E_1 from Eq. (25). Keeping only the terms linear in E_1 we get

$$E_1(\mathbf{r},t)=C\int d^2r'Q(\mathbf{r},\mathbf{r}')x'^{1/n-1}\dot E_1(\mathbf{r}',t) \tag{40}$$

with $C=\mu_0 J_c/(nE_c^{1/n}\dot B_a^{1-1/n})$. This linear equation is solved by the ansatz $E_1(x,y,t)=g(x,y)\exp(-t/\tau)$. The profile $g(x,y)$ and the time constant τ follow from the linear eigenvalue equation

$$g_\nu(\mathbf{r})=-\lambda_\nu\int d^2r'Q(\mathbf{r},\mathbf{r}')x'^{1/n-1}g_\nu(\mathbf{r}), \tag{41}$$

where the eigenvalues λ_ν have to equal C/τ_ν, thus $\tau_\nu=C/\lambda_\nu$. We are interested in the relaxation mode with the longest time constant τ_1 corresponding to the lowest eigenvalue λ_1. We thus find at $t\gg\tau_1$

$$E(\mathbf{r},t)=x\dot B_a-\text{const}\;g_1(x,y)\exp(-t/\tau_1), \tag{42}$$

$$\tau_1 = \frac{C}{\lambda_1} = \frac{\mu_0 J_c}{n \dot{B}_a \lambda_1} \left(\frac{\dot{B}_a}{E_c} \right)^{1/n}, \tag{43}$$

where λ_1 and $g_1(x,y)$ are the lowest eigenvalue and eigenfunction of Eq. (41) and the constant has to be determined from the full nonlinear equation (25). This exponential approach to the saturation of E, and thus also of J and of the magnetic moment M, is quantitatively confirmed by our computations in Sec. V.

D. Linear response: Eigenvalue problems

Writing $E = \rho J$ we may put the equation of motion (6) for the current density $J(x,y,t)$ into the form

$$\frac{\rho}{\mu_0} J(\mathbf{r},\mathbf{t}) = \int_S d^2 r' Q(\mathbf{r},\mathbf{r}') \dot{J}(\mathbf{r}',t) + x \dot{H}_a(t) \tag{44}$$

with $H_a = B_a/\mu_0$ and $\rho/\mu_0 = D$ the diffusion coefficient of flux. We discuss now three cases where the linear response J to a time dependent applied field $H_a(t)$ can be obtained from an eigenvalue problem, which is easily solved by finding the eigenvectors of the matrix $Q_{ij} = Q_{\rm sym}(\mathbf{r}_i, \mathbf{r}_j)$ introduced in Sec. IV A. In these three cases, respectively, the general resistivity ρ in (44) is either (1) ohmic (linear, real, frequency independent); (2) linear, complex, and dispersive, $\rho = \rho_{ac}(\omega)$; or (3) arbitrarily nonlinear, $\rho = \rho(J) = E(J)/J$.

I present here the main formulas, detailed numerical results will be given elsewhere.

1. Ohmic bar in switched field

When the applied field $H_a(t)$ changes abruptly from one constant value to another at time $t = 0$, e.g., by switching it on or off, one has $\dot{H}_a(t) = 0$ at $t \neq 0$. Equation (44) is then solved by a linear superposition of relaxing eigenmodes

$$J(x,y,t) = \sum_{\nu=1}^{\infty} c_\nu f_\nu(x,y) e^{-t/\tau_\nu}. \tag{45}$$

The amplitudes c_ν as usual are obtained from the initial condition at $t = 0$ and the $f_\nu(x,y)$ are the eigenfunctions of the linear equation (30), which for rectangular bars may be written in terms of $Q_{\rm sym}$ (9),

$$f_\nu(\mathbf{r}) = -\Lambda_\nu \frac{4\pi}{S'} \int_0^a dx' \int_0^b dy' Q_{\rm sym}(\mathbf{r},\mathbf{r}') f_\nu(\mathbf{r}'). \tag{46}$$

The time constants τ_ν are obtained by equating the prefactors of (46) and of (44) with (45) inserted, $4\pi\Lambda_\nu/S' = \mu_0/(\rho\tau_\nu)$, yielding

$$\tau_\nu = \frac{\mu_0 S'}{4\pi\rho\Lambda_\nu}. \tag{47}$$

Note that only the ratio Λ_ν/S' enters in (46) and (47). To get dimensionless eigenvalues Λ_ν we have introduced in (30) and (46) the arbitrary area S'. As shown in Sec. IV B, it is convenient to choose for S' the specimen cross section $S' = S = 4ab$ if one considers the perpendicular limit $b \ll a$, i.e., a thin strip in perpendicular field. This yields the time constants $\tau_\nu = \mu_0 ab/(\pi\rho\Lambda_\nu)$ with $\Lambda_\nu \approx 0.6385 + \nu - 1$, $\nu = 1,2,\ldots$, as in Refs. 13 and 31.

For the longitudinal limit $b \gg a$ of a slab in parallel field, the eigenvalues of the integral equation (30) are obtained from the equivalent linear differential equation with boundary conditions [cf. the similar Eq. (37)],

$$f_\nu''(x) = -k_\nu^2 f_\nu(x), \quad f_\nu(0) = f_\nu'(a) = 0, \tag{48}$$

yielding $f_\nu = \sin k_\nu x$ and $k_\nu = \pi(\nu - 1/2)/a$, $\nu = 1,2,\ldots$. Equating the prefactors of (46) and (48), $4\pi\Lambda/S' = k_\nu^2$, we obtain the time constants (47), $\tau_\nu = \mu_0/(\rho k_\nu^2) = \mu_0 a^2/[\pi^2(\nu - 1/2)^2\rho]$ as in Refs. 13 and 15. As stated in Sec. IV B, the choice $S' = 16a^2/\pi$ appears natural in this parallel limit since it yields $\Lambda_\nu = (2\nu - 1)^2 = 1,9,25,\ldots$. A convenient interpolation to all side ratios b/a is the choice $S' = 4ab/(1 + \pi b/4a)$ as above.

2. Linear complex ac susceptibility

The linear magnetic response of a bar with general complex resistivity $\rho_{ac}(\omega)$ (Refs. 26,32 and 53–58) in a perpendicular ac field $H_a(t) = H_{\rm dc} + H_0 \exp(i\omega t)$ may be obtained from Eq. (44) using the method presented in Ref. 31. A convenient complex frequency variable is

$$w = \frac{i\omega\mu_0 S'}{4\pi\rho_{\rm ac}(\omega)} = i\omega\tau(\omega), \tag{49}$$

where τ is a time constant which in general is complex; only for ohmic ρ is τ a real relaxation time. With the same choices as above, $S' = 4ab$ $(b \ll a)$ and $S' = 16a^2/\pi$ $(b \gg a)$, one gets $w = i\omega\mu_0 ab/\pi\rho_{ac}$ for thin strips (as in Ref. 31) and $w = i\omega\mu_0 4a^2/\pi^2\rho_{ac}$ for slabs, and the dissipative part χ'' of the ac susceptibility $\chi = \chi' - i\chi''$ has its maximum at $|w| \approx 1$ for all side ratios b/a.

In terms of the eigenvalues Λ_ν and eigenfunctions $f_\nu(x,y)$ of Eqs. (30) or (46), with the normalization

$$\frac{4\pi}{S'} \int_S d^2 r f_\mu(\mathbf{r}) f_\nu(\mathbf{r}) = \delta_{\mu\nu}, \tag{50}$$

and with the dipole moments

$$b_\nu = \frac{4\pi}{S'} \int_S d^2 r x f_\nu(\mathbf{r}), \tag{51}$$

the magnetic moment per unit length of the bar becomes

$$m(t) = \int_S d^2 r x J(\mathbf{r},t) = m(\omega) e^{i\omega t}, \tag{52}$$

$$m(\omega) = H_0 w \sum_\nu \frac{\Lambda_\nu b_\nu^2}{w + \Lambda_\nu}. \tag{53}$$

The magnetic susceptibility $\chi(\omega) = -m(\omega)/m(\infty)$ of bars with $\rho = \rho_{\rm ac}(\omega)$ in a perpendicular ac field is thus

$$\chi(\omega) = -w \sum_\nu \frac{\Lambda_\nu b_\nu^2}{w + \Lambda_\nu} \Big/ \sum_\nu \Lambda_\nu b_\nu^2. \tag{54}$$

This general expression applies to bars with arbitrary cross section in a perpendicular ac field, also to cylinders. In the limits $b \ll a$ and $b \gg a$ it reproduces the susceptibility of thin strips[31] and of slabs[16,26,31] and yields interesting corrections

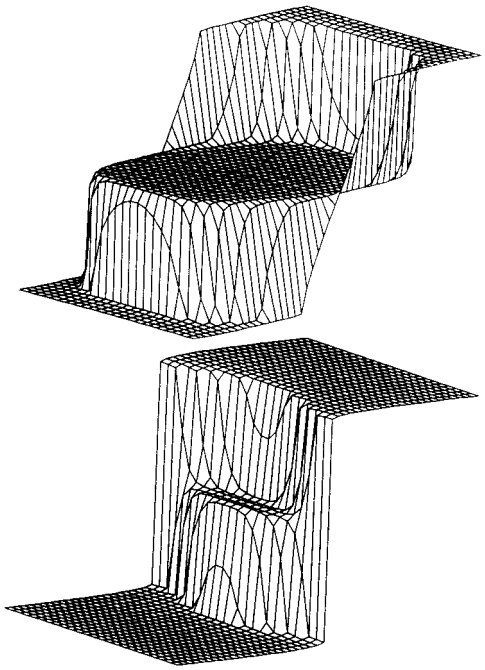

FIG. 4. Profiles of the current density $J(x,y)$ in a superconducting bar of side ratio $b/a=0.5$ in an increasing perpendicular field H_a at $H_a/H_p=0.2$ (top) and 0.8 (bottom) in units of the penetration field $H_p=0.540J_c a$ (64) for creep exponent $n=51$ on a grid of 24×12 points. Notice the penetrating saturation to $J=\pm J_c$, the current-free zone $J=0$ in the center, and the abrupt jump of J at the two ends of the central line $x=0$ in the lower plot.

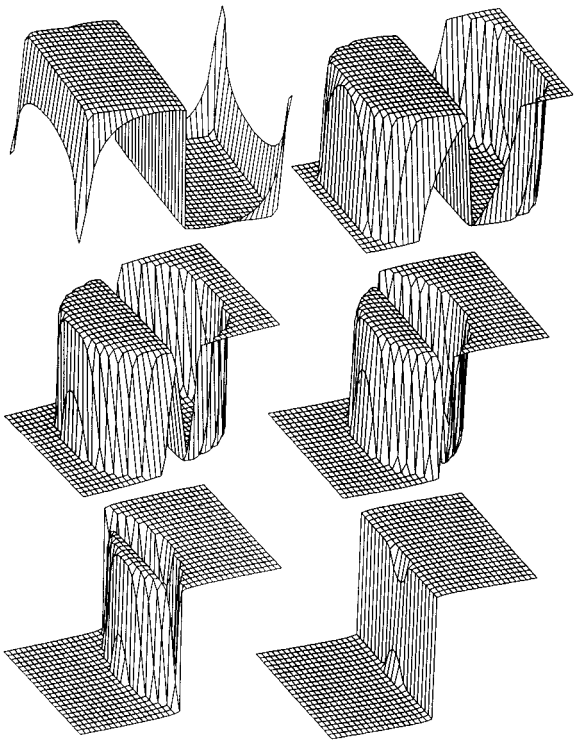

FIG. 5. Profiles of the current density $J(x,y)$ when H_a is decreased from $+H_p$ (64) to $-H_p$ for side ratio $b/a=0.5$ and exponent $n=51$ as in Fig. 4, but on a grid of only 20×11 points. From left to right and top to bottom one has $H_a/H_p=0.95$, 0.7, 0.4, 0, -0.4, -0.9.

due to the nonzero thickness of the strip or slab. In particular, for $b\ll a$ the permeability $\mu(\omega)=1+\chi(\omega)$ at large frequencies ($|w|\gg1$) changes from ''perpendicular''to ''parallel'' behavior,

$$\mu(\omega)=(2/\pi w)\ln(16w), \quad \omega\ll\omega_0, \tag{55}$$

$$\mu(\omega)=c/w^{1/2}, \quad \omega\gg\omega_0, \tag{56}$$

where ω_0 and the constant c depend on b/a. The real and imaginary parts of χ follow from (54) to (56) with w from (49) inserted. More details and numerical results for arbitrary side ratio b/a and the extension to discs and cylinders in an axial ac field will be given elsewhere.[43]

3. Linear ac response during creep

Very recently it was shown[38] that a superconductor (or nonlinear conductor) which performs flux creep away from the fully penetrated critical state exhibits a linear response to a small ac magnetic field. Extending this theory to the present geometry, I find that the linear ac susceptibility during creep is given by the same expressions (54)–(56) but with different constants Λ_ν, b_ν, ω_0, and c and, most remarkably, with the complex frequency variable w (10) replaced by the imaginary variable $i\omega t$ where t is the time which has elapsed since creep has started. This means that the linear $\chi(\omega)$ during creep is *universal*, depending only on the geometry and the creep time, but not on temperature, applied or internal dc magnetic fields, or any material parameter. The universal expressions for χ apply only for not too small frequencies $\omega\gg1/t$. Therefore, the maximum in the dissipative part χ'' of $\chi=\chi'-i\chi''$ (54) occurring at $|w|\approx1$ (if S' is choosen as suggested above) has no equivalent in the linear susceptibility during creep.

4. Flux penetration in the Meissner state

For a superconductor in the Meissner state with magnetic penetration depth λ the London equation $A=-\mu_0\lambda^2 J$ in our bar geometry may be written as

$$\lambda^2 J(\mathbf{r})=\int_S d^2r'\,Q(\mathbf{r},\mathbf{r}')J(\mathbf{r}')+xH_a, \tag{57}$$

cf. Eq. (2). In the matrix formulation on a grid (x_i,y_i) of Sec. IV A, Eq. (57) reads

$$\lambda^2 J_i=\sum_j Q_{ij}J_j+x_jH_a. \tag{58}$$

This matrix equation is solved for the current density $J_i=J(x_i,y_i)$ by inverting the matrix $Q_{ij}-\lambda^2\delta_{ij}$, cf. also Eq. (24),

$$J_i=H_a\sum_j (\lambda^2\delta_{ij}-Q_{ij})^{-1}x_j. \tag{59}$$

Thus the London penetration of a perpendicular magnetic field H_a into a bar of arbitrary cross section is obtained by finding the eigenvalues of the matrix $Q_{ij}=Q(\mathbf{r}_i,\mathbf{r}_j)$

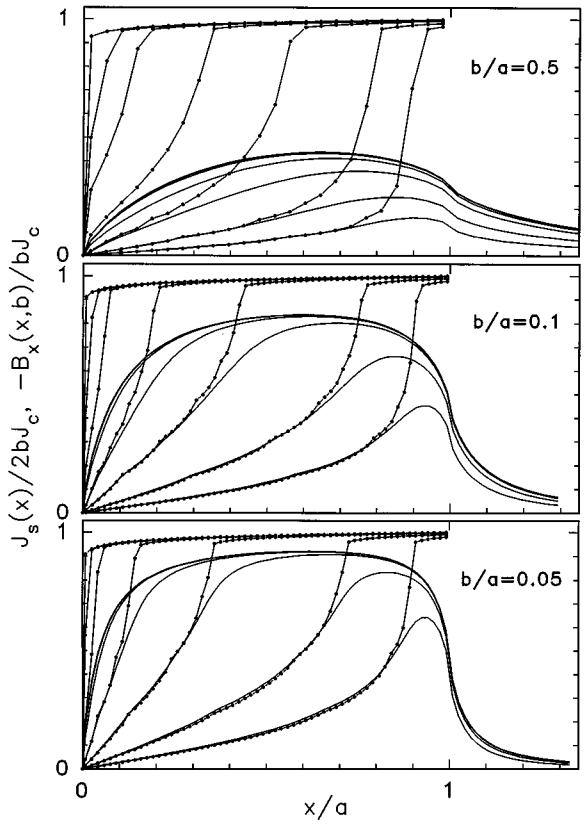

FIG. 6. The sheet current $J_s(x)$ (15) (current density integrated over the thickness) for flat bars with side ratios $b/a=0.5$, 0.1, and 0.05 (from top to bottom) and exponent $n=51$ during flux penetration, plotted in units $J_c a$ for applied fields $H_a/H_p=0.1$, 0.2, 0.4, 0.6, 0.8, 0.9, and 1 (from right to left, solid line with dots). H_p is the penetration field (64), $H_p/J_c a=0.540$, 0.207, and 0.125. The solid lines give the parallel component of the magnetic field at the surface, $B_x(x,b)$, which for thin strips ($b \ll a$) should coincide with $-J_s/2$ for $|x|<a$ and vanish for $|x|>a$ (i.e., away from the strip). As seen in this plot, the abrupt jump in J_s from J_c to 0 at the specimen edge $x=a$ causes a jump in B_x which is smeared due to finite thickness 2b.

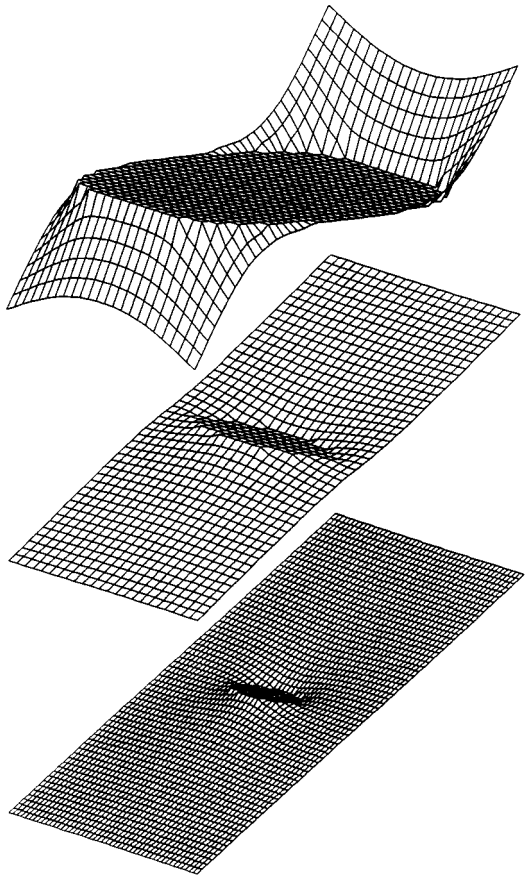

FIG. 7. Profiles of the electric field $E(x,y)$ during flux penetration into a superconducting bar of side ratio $b/a=0.5$ and exponent $n=51$ as in Fig. 4, for the same values $H_a/H_p=0.2$ (top) and 0.8 (middle and bottom). The top and middle $E(x,y)=J^n \mathrm{sgn} J$ are computed as the 51st power of the $J(x,y)$ plotted in Fig. 4 and are thus defined only inside the bar, $|x|\leqslant a$ and $|y|\leqslant b$. The bottom $E(x,y)$ is the same as the middle $E(x,y)$ but is plotted in the larger region $|x|\leqslant 1.4a$ and $|y|\leqslant 2b$ (33×24 grid points) covering also some space outside the superconductor; here E was computed from $E=-\dot{A}$. The specimen edges cannot be seen in the bottom plot since $E(x,y)$ is smooth at the specimen surfaces.

$=\ln|\mathbf{r}_i-\mathbf{r}_j|/2\pi$. The magnetic moment is then obtained as $m=\Sigma_i x_i J_i$. This very effective computational method is easily extended to other geometries. In the limit $\lambda\to 0$, Eq. (59) yields the surface screening currents, which in this 2D problem may also be calculated by the method of conformal mapping. The ideal diamagnetic moment is computed in Sec. V F.

V. FLUX PENETRATION AND CREEP

In this section I present a selection of useful results computed mainly by time integration of Eq. (24) for superconductors of rectangular cross section with weak creep. More results will be given elsewhere.[43] In all figures the orientation of the applied field (y axis) is vertical.

A. Field of full penetration

One characteristic quantity in the Bean model for various geometries is the field value H_p at which in a gradually increasing applied field $H_a(t)$ the magnetic flux has penetrated to the center and the current density has reached its saturation value J_c in the entire specimen. For slabs and strips of rectangular cross section $2a\times 2b$ this field of full penetration in the parallel and perpendicular limits is given by

$$H_p \approx J_c a, \quad b \gg a, \tag{60}$$

$$H_p \approx J_c (2b/\pi)\ln(2a/b), \quad b \ll a. \tag{61}$$

The parallel H_p (60) is obvious from the constant slope $|dH/dx|=J_c$ of the penetrating field and the boundary condition $H=H_a$ at $x=\pm a$. The penetration field (61) for the perpendicular geometry is less obvious. It follows from the Bean solution[10–12] for thin strips by introducing an inner cutoff such that full penetration is reached when the width of the flux-free central zone $2a/\cosh(H_a\pi/J_c d)$ has decreased to the specimen thickness $d=2b$. Our computations for small but finite side ratio b/a confirm this cutoff argument. More-

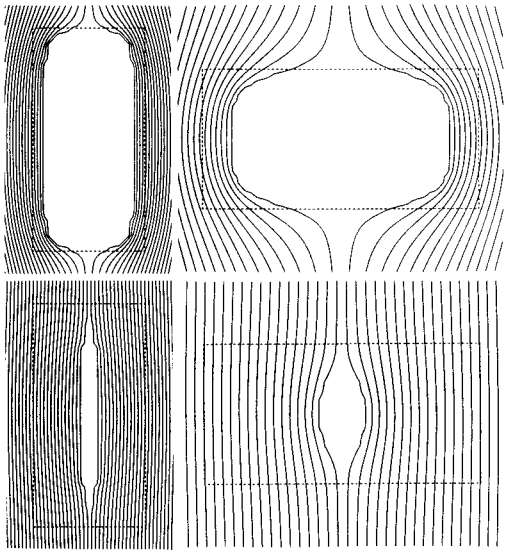

FIG. 8. Electric field $E(x,y)$ during flux penetration at constant ramp rate $\dot{H}_a$ in bars with side ratios $b/a=2$ (left) and $b/a=0.5$ (right) at two field values $H_a/H_p=0.2$ (top) and $H_a/H_p=0.8$ (bottom) where H_p is the penetration field (64) ($n=51$, $H_p/J_c a=0.862,\ 0.540$). The plotted lines of constant E look similar as the magnetic field lines of Fig. 9 below, but they are nearly equidistant, while the magnetic field lines inside the bar have nearly linearly varying distance when the gradient $\partial B_y/\partial x$ is nearly constant.

over, it appears that our computed values of H_p for all side ratios $0.005\leqslant b/a\leqslant 6$ are fitted to an accuracy of better than 2% by a compact expression which has the correct limits (60) and (61),

$$H_p = J_c a \tanh\left[\frac{2b}{\pi a}\ln\left(1.47+\frac{2.68a}{b}\right)\right]. \tag{62}$$

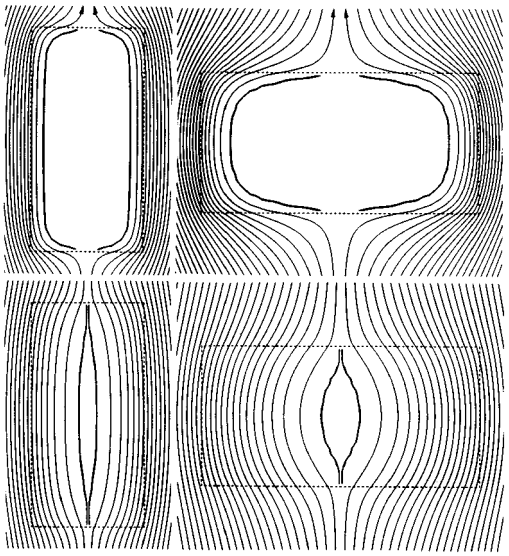

FIG. 9. Field lines of the magnetic field $B(x,y)$ during flux penetration into bars with side ratios $b/a=2$ and $b/a=0.5$ at two field values $H_a/H_p=0.2$ and $H_a/H_p=0.8$, $n=51$, the same cases shown in Fig. 8. The bold lines indicate the flux and current fronts shown also in Fig. 2.

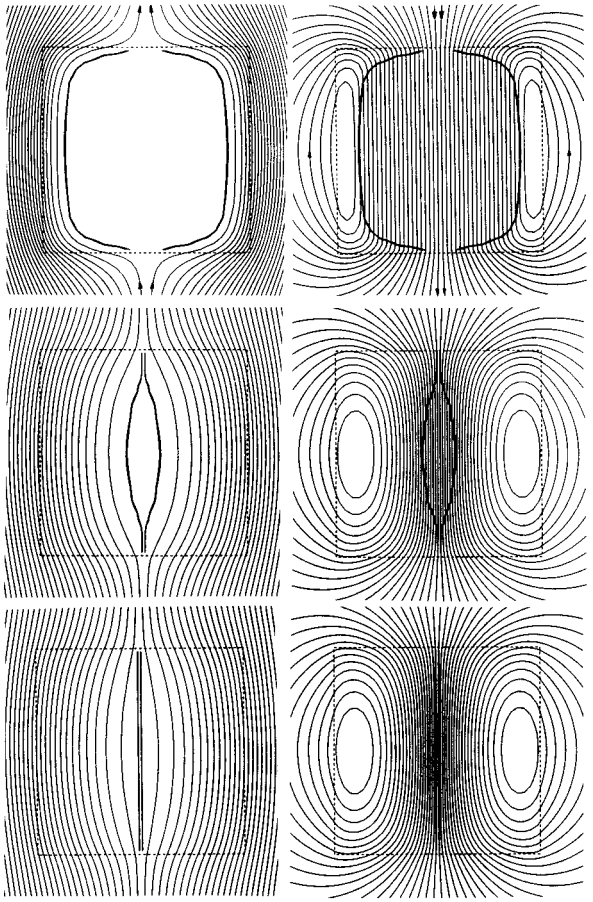

FIG. 10. Magnetic field lines for a square bar ($b=a$) in an increasing perpendicular field H_a for $H_a/H_p=0.2$, 0.8, and 1 (full penetration) with $H_p=0.715J_c a$ from (64), $n=51$. Left: total magnetic field flowing around the flux-free core. Right: the magnetic field caused by the currents in the bar, $B-B_a$. This is also the field in a remanent state with the same degree of flux penetration, which may be reached after field cooling by decreasing H_a to zero. For full penetration, $H_a\geqslant H_p$ (bottom right), the plotted field lines of $B-B_a$ coincide with the lines of constant electric field during flux creep, (Ref. 49) cf. Sec. IV D. The bold lines indicate the flux and current fronts, cf. Fig. 2.

Figure 1 shows computed penetration fields in units $J_c a$ at various values of the side ratio b/a of rectangular bars in a perpendicular field. It can be seen that for large exponent $n=101$ these data are perfectly fitted by formula (62). At smaller exponents the penetration field is reduced due to flux creep, which allows the flux front to reach the specimen center earlier than in ''hard'' Bean superconductors with $n=\infty$.

Here the principal problem arises how to define the field of full penetration when the creep exponent is $n<\infty$. As shown in Sec. IV C, the magnetic saturation at constant ramp rate $\dot{B}_a$ is approached only gradually, with an exponential time law Eq. (42), see also Sec. V F. In Fig. 1 H_p is defined as the field at which the current profiles $J(x,y)$ become nearly constant along the field (y) direction, such that the mean square difference

$$s=\frac{1}{a}\int_0^a [J(x,a)-J(x,0)]^2 dx \tag{63}$$

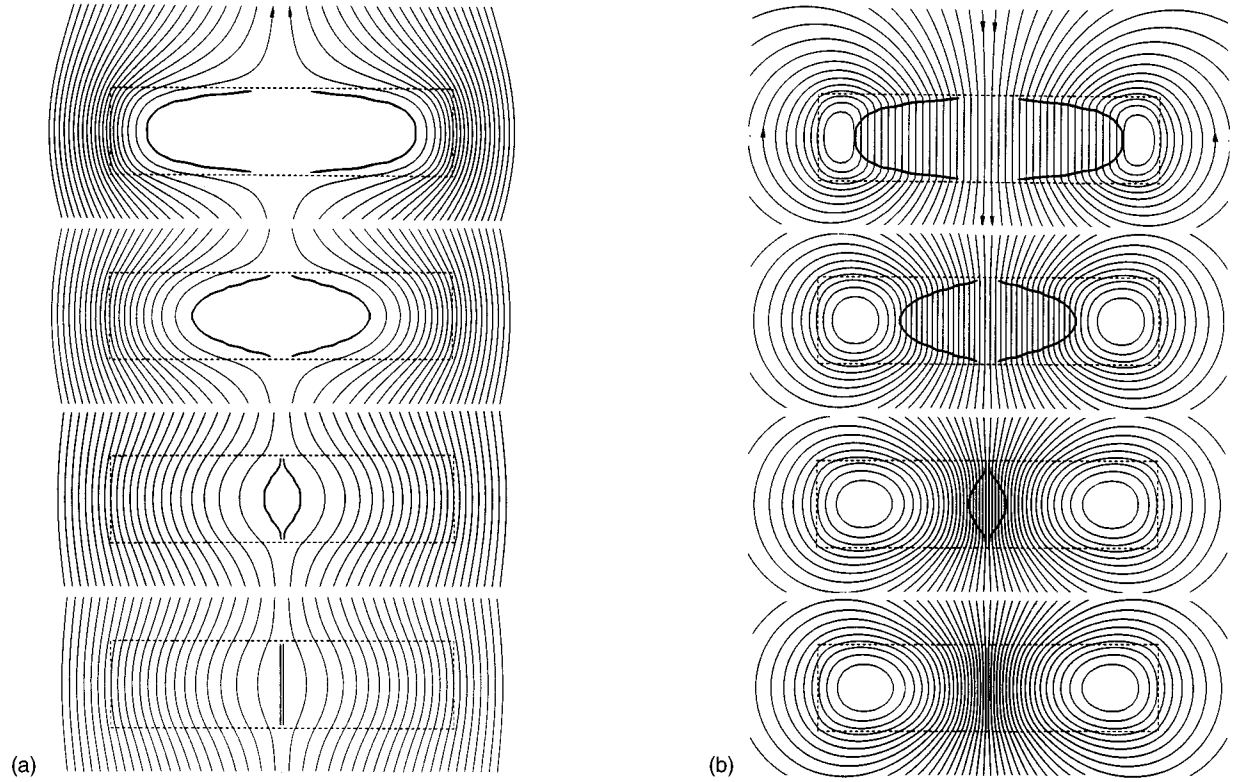

FIG. 11. Magnetic field lines during penetration of perpendicular flux into a thick strip with $b/a=0.25$ at applied fields $H_a/H_p=0.2$, 0.4, 0.8, and 1, $H_p=0.374J_c a$, $n=51$. (a) total field $B(x,y)$. (b) current-caused field $B(x,y)-B_a$, or field in the remanent critical state. The flux front is shown as bold line.

becomes smaller than 5×10^{-6}. This is a quite sharp criterion: The computed quantity s, and also the difference between the magnetic moment $m(t)$ and its saturation value $m(\infty)=m_{\rm sat}$, Eq. (69) below, decrease exponentially in time, and thus in $H_a=t\dot{H}_a$, over at least seven decades in a narrow field interval if n is large.

The slight reduction of the penetration field with decreasing creep exponent n is fitted to a good approximation by shifting the entire curve H_p (61) plotted versus $\ln(b/a)$, horizontally as shown in Fig. 1. For $5\leqslant n<\infty$ this fit yields

$$H_p\approx J_c a\tanh\left[\frac{2x}{\pi}\ln\left(1.47+\frac{2.68}{x}\right)\right],$$

$$x=\frac{b}{a}\exp\left(-\frac{2.2}{n}+0.022\right). \tag{64}$$

For smaller exponents $n<5$ the definition of H_p is not unique since creep into the saturation state is slow.

The computed penetration field (62) has to be compared with the exact analytical expression for H_p given by Forkl.[59] The applied field at which the magnetic field reaches the center of an arbitrarily shaped Bean superconductor can be obtained from the Biot-Savart law by calculating the field $H(\mathbf{r})$ caused by the critical currents. In the Bean critical state the magnitude of $J(\mathbf{r})$ equals J_c and its direction depends on the specimen shape as discussed, e.g., in Refs. 1–6,21–23, and 60. At the moment when the flux front has reached the specimen center $\mathbf{r}=0$, the current-caused field $H(0)$ there should exactly compensate the applied field H_a. From this argument Forkl[59] obtains for a rectangular bar and for a circular disk of constant thickness $2b$ and radius a the perpendicular penetration fields

$$H_p=J_c\frac{b}{\pi}\left[\frac{2a}{b}\arctan\frac{b}{a}+\ln\left(1+\frac{a^2}{b^2}\right)\right]\quad\text{(bar)}, \tag{65}$$

$$H_p=J_c\,b\ln\left[\frac{a}{b}+\left(1+\frac{a^2}{b^2}\right)^{1/2}\right]\quad\text{(disk)}. \tag{66}$$

The general expression (65) has the limits

$$H_p=J_c a(1-a/\pi b),\quad b\gg a, \tag{60a}$$

$$H_p=J_c(2b/\pi)\ln(ea/b),\quad b\ll a. \tag{61a}$$

This means the estimated factor 2 in the logarithm in (61) has the exact value $e=2.718$, which is close to the fitted value 2.68 in (62) and (64).

As can be seen in Fig. 1, the guessed fit function (62) for $H_p(b/a)$ coincides with the exact analytical result (65) within line thickness for all side ratios $b/a\leqslant1.5$. At larger b/a values, the H_p expected for finite creep exponents n can be larger or smaller than H_p (65) depending on the criterion chosen to define full penetration. In principle, for any $n<\infty$ the penetration field also should slightly depend on the ramp rate $\dot{B}_a$, which in our computation is chosen equal to unity in units $a=J_c=E_c=\mu_0=1$. Moreover, the saturated magnetic moment $m_{\rm sat}$ itself depends on $\dot{B}_a$ when $n<\infty$. This may be seen as follows.

B. Saturated state

When the applied field is increased with constant ramp rate $\dot{B}_a$ then eventually the current density saturates such that $\dot{J}=0$. It follows then from Eq. (6) that the electric field saturates to the profile $E(\mathbf{r},\infty)=x\dot{B}_a$. From this stationary E we get the stationary J by inverting the given $E(J)$ law. For the power law (1) and constant $\dot{B}_a$ one obtains thus for the fully saturated (critical) state, using $m=4b\int_0^a xJ(x)dx$ (Sec. V F),

$$E=E_{\rm sat}(x)=x\dot{B}_a=E_c(J_{\rm sat}/J_c)^n, \tag{67}$$

$$J=J_{\rm sat}(x)=J_c\left(\frac{\dot{B}_a a}{E_c}\right)^{1/n}\left(\frac{x}{a}\right)^{1/n}, \tag{68}$$

$$m=m_{\rm sat}=2J_c ba^2\left(\frac{\dot{B}_a a}{E_c}\right)^{1/n}\frac{2n}{2n+1}. \tag{69}$$

From Eqs. (67)–(69) we notice several remarkable facts, which are all confirmed by our computations.

(a) The profiles of the saturated current density and electric field depend only on the coordinate x, but not on y and not on the specimen height $2b$. They do not depend on the shape of the bar cross section at all.

(b) The general results (67)–(69) depend only on the combination E_c/J_c^n, but in the limit $n\to\infty$ only J_c matters. For large creep exponents $n\gg 1$ the weak x dependence of J may be disregarded and one has $J_{\rm sat}\approx J_c$ and $m_{\rm sat}\approx 2ba^2J_c$ as predicted by Bean.[1]

(c) For general creep exponent $n<\infty$ the saturation magnetization depends slightly on n and on the ramp rate $\dot{B}_a$. The saturation is reached exponentially fast as shown in Sec. IV C.

C. Current density

Figure 2 shows the fronts of penetrating flux in rectangular bars of various side ratios b/a in an increasing perpendicular applied field H_a. In the lens-shaped region between the two fronts one has $B=0$ and $J=0$, and outside this zone $J=\pm J_c$. This means one has a current-caused Bean critical state across the thickness, with full penetration of the current in the outer zone $|x|>x_0$ and partial penetration in the inner region $|x|<x_0$. For fields H_a below some value $H_{\rm det}$ the flux- and current-free zone meets the surface at the two points (or lines along z) $x=0$, $y=\pm b$. The current density $J(x,y)$ at the surfaces $y=\pm b$ thus goes smoothly through zero with finite slope, as it does on the entire central line $x=0$. For not too thick strips the shape of this inner zone where $\mathbf{B}=0$ and $J=0$, and of the sickle-shaped outer zones where $J=\pm J_c$, follows from the known analytical expression for the sheet current $J_s(x)$ (15) of thin Bean strips,[10–12]

$$J_s(x)=\frac{2J_c d}{\pi}\arctan\left[\left(\frac{a^2-x_0^2}{x_0^2-x^2}\right)^{1/2}\frac{x}{a}\right] \tag{70}$$

for $0\leqslant x\leqslant x_0$ and $J_s(x)=J_c d$ for $x_0\leqslant x\leqslant a$, and $J_s(-x)=-J_s(x)$, where $x_0=a/\cosh(\pi H_a/J_c d)$ is the position of the flux front on the middle plane $y=0$ and $d=2b$ is the thickness of the strip. For $x_0<a/2$ one has $J_s(x)\approx(2J_c d/\pi)\arcsin(x/x_0)$. Since the current density is either 0 or $\pm J_c$, the boundary of the current-free zone in the half strip $x>0$ takes the form

$$y(x)=\pm b\left(1-\frac{J_s(x)}{J_c d}\right)\approx b\frac{2}{\pi}\arccos\frac{x}{x_0}. \tag{71}$$

This analytical estimate is compared with the numerically obtained flux fronts in Fig. 3. As expected, the agreement is best near the flat surfaces $y=\pm b$ but away from the edges $x=\pm a$ and from the center $x=0$. In general, the correct numerical result exhibits a faster penetration: The low-field flux front is flatter and nearly parallel to the edges and has penetrated deeper than predicted by (71). This behavior of the flux fronts will be modified further when in future computations a finite lower critical field H_{c1} can be accounted for, which leads to an edge barrier.[47,18,19,26] Next we discuss the deviation from the analytical front (71) near the specimen center.

At larger fields $H_a>H_{\rm det}$ the central flux-free zone detaches from the surface and becomes isolated. This detachment occurs when the boundary of the flux-free zone at the surface $y=\pm b$ has a slope of approximately 45°. The current density now jumps abruptly from $+J_c$ to $-J_c$ on the two sections of the central line (or plane) $x=0$ which connect this lens-shaped zone with the surfaces. This jump can be seen in the 3D plots of Fig. 4. From Fig. 3 one sees that for $b\geqslant a/2$ the detachment field is approximately $H_{\rm det}\approx H_p/2$ with H_p from (64) and for $b/a=0.25$ (0.1225, 0.0625) one has $H_{\rm det}/H_p\approx 0.6$ (0.7, 0.8). For $b/a\to 0$ one has $H_{\rm det}/H_p\to 1$. Notice that the computed exact flux front of Figs. 2 and 3 differ from the concentric ellipsoids which were assumed in the analytical calculations of Refs. 4 and 5.

The curved flux fronts in Fig. 2 were computed from Eq. (24) on grids of $N=N_xN_y\approx 600$ points for a creep exponent $n=21$. They are defined as the two lines (or planes) where $J(x,y)=\pm 0.5J_c$. The two straight parallel contour lines visible in the center where J jumps from $+J_c$ to $-J_c$, ideally should occur at $x=\pm a/2^n$, cf. Eq. (68), but in these figures they appear at $x=\pm 0.25/N_x$ since on the grid the jump goes from $x_1=0.5/N_x$ to $-x_1$. Apart from this detail the contours obtained for different exponents $n\geqslant 11$ and different grid spacing practically coincide. Similar flux fronts for the Bean model were recently computed by Prigozhin[61] from a variational principle, and from differential equations by Becker *et al.*[62] The detachment of the Bean flux fronts from the surface was also seen in computations of cylindrical wires in transverse field[63,64] and in spheres and spheroids.[65,66]

When the applied field is decreased from $H_a=H_p$ to $-H_p$, the new fronts of penetrating flux and current of opposite sign have the same shape as the fronts depicted for the virgin magnetization curve in Fig. 2. At these new fronts J jumps from $+J_c$ to $-J_c$; the natural definition of these front lines (or planes) is thus $J(x,y)=0$. When $H_a=-H_p$ is reached one arrives again at the critical state but with J and $\mathbf{B}$ having reversed sign. When H_a is decreased from $H_0\geqslant H_p$ to $-H_0$ the new fronts $y_\downarrow(x)$ follow from the virgin fronts $y(x)$ by the relation

$$y_\downarrow(x,H_a)=y\left(x,\frac{H_0-H_a}{2}\right). \tag{72}$$

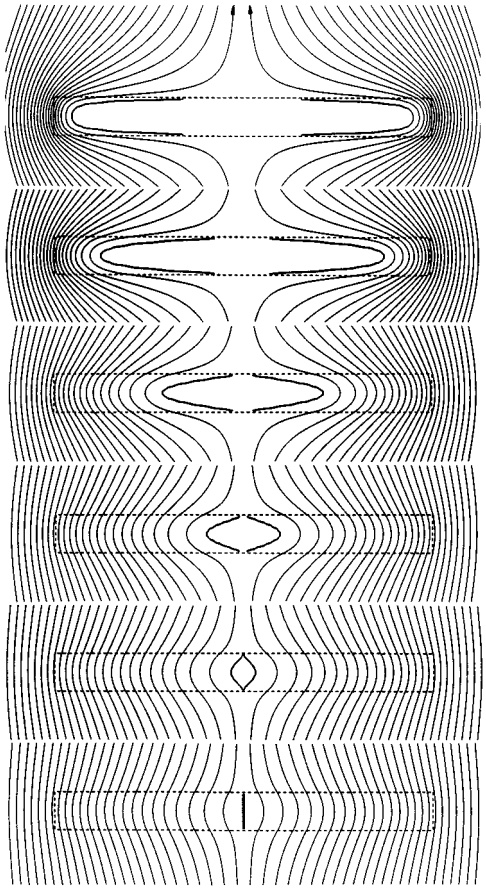

FIG. 12. Magnetic field lines during penetration of perpendicular flux into a thinner strip with $b/a=0.1$ at applied fields $H_a/H_p=0.1$, 0.2, 0.4, 0.6, 0.8, and 1 (from top), $H_p=0.207J_c a$, $n=51$. The flux front is shown as bold line.

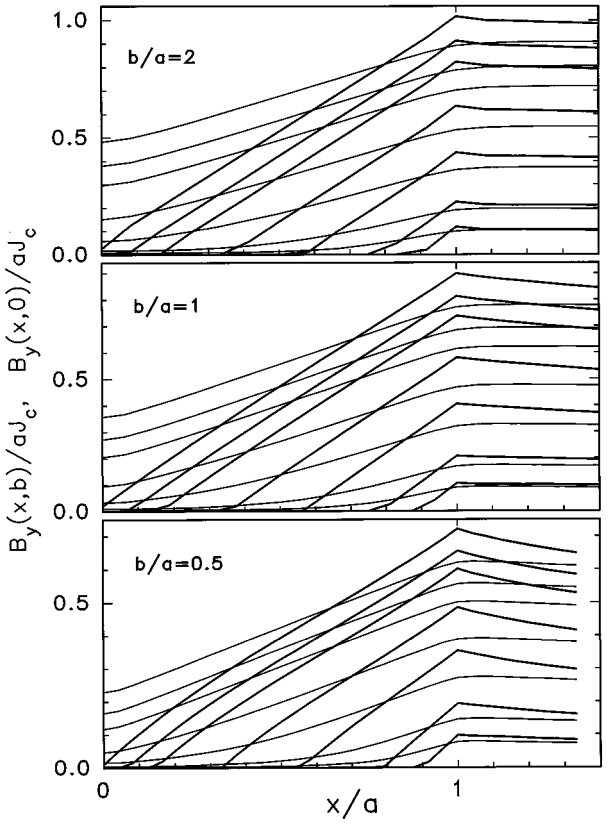

FIG. 13. Profiles of the perpendicular flux density $B_y(x,y)$ at the surface (thin lines, $y=\pm b$) and central plane (thick lines, $y=0$) of bars with side ratios $b/a=2$, 1, and 0.5 in an increasing perpendicular field $H_a/H_p=0.1$, 0.2, 0.4, 0.6, 0.8, 0.9, 1 ($H_p/J_c a=0.862$, 0.715, 0.540, $n=51$). The corresponding parallel component $B_x(x,b)$ is shown in Fig. 6.

This simple superposition principle applies only to the Bean model, i.e., when J_c is independent of B and n is infinite. The penetration of the reversed flux and current is shown in the 3D plots of Fig. 5. Computing such a half cycle on a 486DX4/100 Personal Computer takes a few minutes.

Figure 6 shows the sheet current $J_s(x)$ (15), i.e., the current density integrated over the thickness. For thin strips $b/a\leqslant 0.05$ the sheet current is related to the parallel field component at the flat surfaces, $B_x(x,\pm b)=\mp J_s/2$, which is also depicted in Fig. 6. The abrupt jumps of $J_x(x)$ at $|x|=x_0$ (flux front) and $|x|=a$ (edge) are smeared in $B_x(x,b)$ over a distance $\approx b$. For $b\ll a$ the computed $J_s(x)$ coincides with formula (70).

D. Electric field

The electric field $E(x,y,t)$ inside the superconductor is obtained by inserting the computed current density $J(x,y,t)$ into the assumed current-voltage law (1), or $E=J^n$ in reduced units. Alternatively, one may obtain E from the time derivative of the vector potential, $E=-\dot{A}$. Both methods give identical results, but $E=-\dot{A}$ yields E also *outside* the specimen. We remind that J, E, and A are directed along z for our bar. Figure 7 shows E during increase of the applied field H_a for the same parameters $b/a=0.5$, $n=51$, and $H_a/H_p=0.2$ and 0.8 used for the current density in Fig. 4. The upper two plots $E(x,y)$ in Fig. 7 thus in principle contain the same information as the plots $J(x,y)$ in Fig. 4 since $E=J^n$. Note that $E(x,y)$ is a smooth continuous function near the specimen edges, where only $\nabla^2 A=-\mu_0 J$ has a discontinuity. Far from the specimen, or after full penetration, one has $E=\dot{B}_a$.

The lines of equal $E(x,y)$ are depicted in Fig. 8 for $b/a=2$ and 0.5, and $H_a/H_p=0.2$ and 0.8. Note that most of the contour lines of E are nearly equidistant, corresponding to the nearly constant slope of E in the 3D plots in Fig. 7. In the absence of an applied field, i.e. in remanent states, the contours lines of $E(x,y,t)$ and $A(x,y,t)$ coincide provided the time dependence separates, $E=f(x,y)g(t)$. This is the case when in the fully penetrated state the applied field is increased further, or when it is held constant to observe flux creep. In these cases the contour lines of E coincide with the magnetic field lines, cf. Fig. 10 below.

E. Magnetic field

Figure 9 shows the magnetic field lines during flux penetration for the same cases as in Fig. 8. The field is applied in vertical direction, as in all figures of this paper. The bold

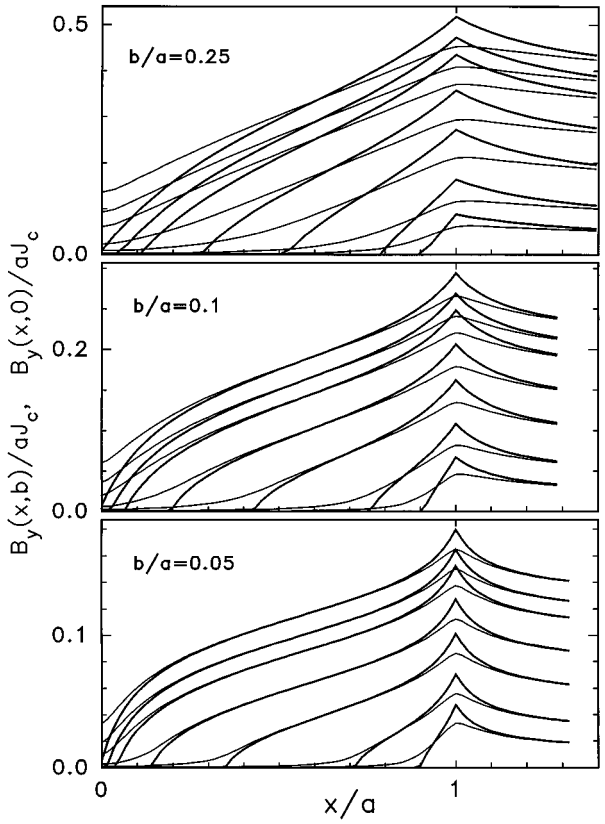

FIG. 14. As Fig. 13, but for thinner strips with side ratios $b/a=0.25$, 0.1, and 0.05 ($H_p/J_ca=0.374$, 0.207, 0.125, $n=51$).

lines are the contour lines where $J=\pm 0.5J_c$ and thus denote the current front as in Fig. 2. More magnetic field lines are depicted in Figs. 10, 11, and 12 for side ratios $b/a=1$ (bar with square cross section), $b/a=0.25$ (thick strip), and $b/a=0.1$ (thin strip). The left column in Fig. 10 shows the field lines of the field $B-B_a$ caused by the currents in the specimen, see also Fig. 11(b). Notice that inside the current-free zone this field is homogeneous and opposed to the applied field, compensating it and creating a field-free zone.

In the particular case of full penetration the current density is known, $J=J_c\mathrm{sgn}x$, and thus $B(x,y)$ can be calculated analytically from the Biot-Savart law.[1–6] In this case the electric field during flux creep, which yields the nearly saturated relaxing current density, is also known analytically, namely, due to the separation of variables t and $\mathbf{r}$ (Sec. IV B) the electric field $E=-\dot{A}$ is proportional to the vector potential A (2) caused by this current.[49] Therefore, the two plots in Fig. 10 (bottom, right) and Fig. 11(b) (bottom) give both the magnetic field lines in the remanent fully penetrated state and the contour lines of the electric field during flux creep or, when B_a is swept, at the moment when B_a goes through zero.

The magnetic field at the surfaces $y=\pm b$ is shown in Fig. 6 (component B_x parallel to the surface) and Figs. 13 and 14 (component B_y perpendicular to the surface) for various values of the increasing B_a. Also shown in Figs. 13 and 14 is the field $B_y(x,0)$ in the central plane where one has $B_x(x,0)=0$ because of symmetry. The central field profile for all side ratios b/a exhibits a sharp cusp at the specimen

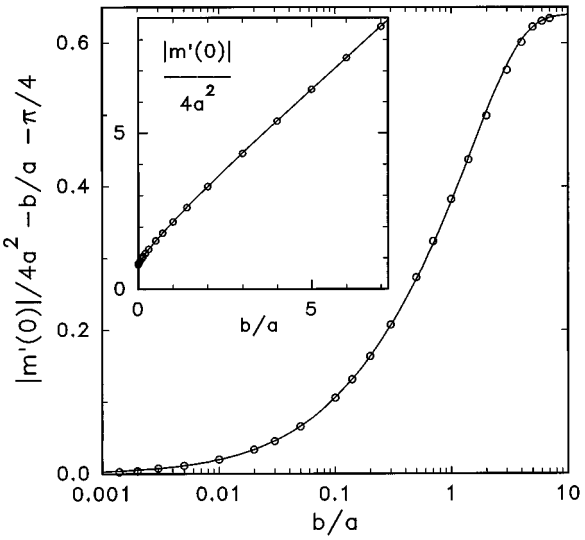

FIG. 15. The initial slope $|m'(0)|$ of the virgin magnetization curve $m(H_a)$ of rectangular bars in perpendicular field H_a, or the ideal diamagnetic moment $m_{\mathrm{scr}}(H_a)=H_am'(0)$, as a function of the side ratio b/a. The circles are computed from Eq. (76) and the line gives the fit formula (77). The inset shows the full $|m'(0)|$ while the main plot shows the difference $|m'(0)|/(4a^2J_c)-b/a-\pi/4$, which vanishes in the perpendicular limit $b\ll a$ and goes to $\gamma\approx 0.64$ in the longitudinal limit $b\gg a$.

edges and a sharp flux front inside which B is exactly zero. These three sharp features are smeared out in the surface field, but for very thin strips this smearing is weak and both field profiles in the center and at the surface nearly collapse into one curve, which coincides with the theoretical profile calculated for thin strips.[11,12]

F. Magnetization curves

The magnetic moment per unit length of a bar with rectangular cross section in a perpendicular applied field $H_a\|y$ is

$$m=\hat{\mathbf{y}}\int_S d^2r\,\mathbf{r}\times\mathbf{J}(\mathbf{r})=4\int_0^a dx\int_0^b dy J(x,y)x. \qquad (73)$$

In (73) the prefactor 1/2 of the definition $mL_z\hat{\mathbf{y}}=(1/2)\int\mathbf{r}\times\mathbf{J}d^3r$ was compensated by the contribution of the U-turning currents at the far away ends of the bar at $z=\pm L_z/2\gg a,b$. The resulting factor of 2 in m was sometimes missed in previous work on slabs.

First I consider the case of ideal screening, where surface screening currents from Eq. (4),

$$J_{\mathrm{scr}}(\mathbf{r})=-H_a\int d^2r'Q^{-1}(\mathbf{r},\mathbf{r}')x' \qquad (74)$$

generate a magnetic field which inside the conductor exactly compensates the applied field H_a and vector potential $A_a=-xB_a$, cf. Eq. (4). From (73) and (74) the ideal diamagnetic moment m_{scr} is obtained, which determines the initial slope $m'(0)=m_{\mathrm{scr}}/H_a$ of the magnetization curve $m(H_a)$ of nonlinear conductors and of superconductors,

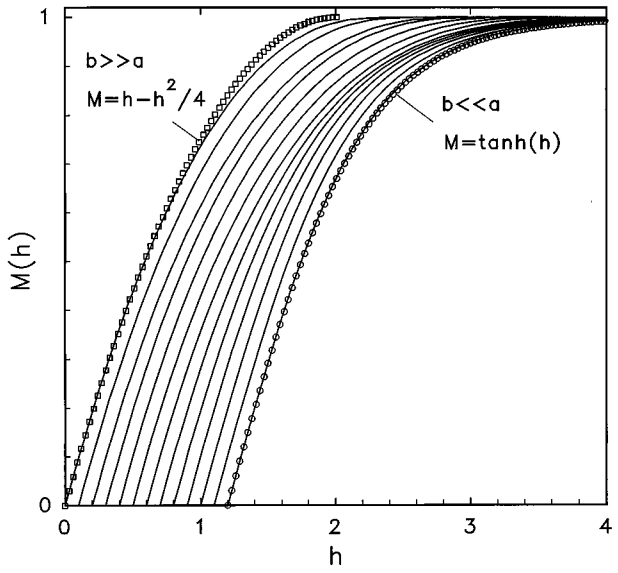

FIG. 16. Normalized virgin magnetization curves $M(h)=-m(H_a)/m_{\rm sat}$, $h=H_a|m'(0)|/m_{\rm sat}$, for rectangular bars with side ratios $b/a=6$, 4, 2, 1.5, 1, 0.7, 0.5, 0.2, 0.1, 0.05, 0.02, 0.01, 0.005 (from left to right, with the origin of each curve slightly shifted, $n=101$). The squares and circles give the parallel and perpendicular limits, $M(h)=h-h^2/4$ and $M(h)=\tanh(h)$, respectively.

$$m'(0)=-\int d^2r\int d^2r'\,xQ^{-1}(\mathbf{r},\mathbf{r}')x'. \tag{75}$$

On our grid of N points $\mathbf{r}_i=(x_i,y_i)$ this reads

$$m'(0)=-\left(\frac{4ab}{N}\right)^2\sum_{ij}x_iQ_{ij}^{-1}x_j, \tag{76}$$

where Q_{ij}^{-1} is the reciprocal matrix of $Q_{ij}=Q(\mathbf{r}_i,\mathbf{r}_j)=\ln|\mathbf{r}_i-\mathbf{r}_j|/2\pi$ (3) or of its symmetrized version (9). Evaluating the sum (76) on a grid with nonequidistant points (more closely spaced near the surface) we get for the rectangular bar the fit with absolute deviation $<3\times10^{-4}$, cf. Fig. 15,

$$\frac{-m'(0)}{4a^2}=\frac{b}{a}+\frac{\pi}{4}+\gamma\tanh\left[\gamma\frac{b}{a}\ln\left(1.7+\frac{1.2a}{b}\right)\right] \tag{77}$$

with $\gamma=0.64$. This approximation has the correct parallel and perpendicular limits, $m'(0)=-4ab$ (the specimen cross section) for $b\gg a$ and $m'(0)=-\pi a^2$ (a circle area) for $b\ll a$.[11–13] Instead from the sum (76), $m'(0)$ also may be computed from Eq. (53) by solving an eigenvalue problem, and it may be calculated analytically by conformal mapping.

Next I discuss the virgin magnetization curves $m(H_a)$ of superconducting bars in an increasing perpendicular field H_a. Above we have already obtained the initial slope $m'(0)$ (77) and saturation value $m(H_a\geqslant H_p)=m_{\rm sat}\approx 2J_cba^2$ (69). One may use these characteristic values to normalize the magnetization curves for various side ratios b/a such that the initial slopes and saturation values equal unity. Writing $m(H_a)=m_{\rm sat}M(h)$, $h=H_a|m'(0)|/m_{\rm sat}$ one has $M'(h)=1$ and $M(h\gg1)=M_{\rm sat}=1$. It turns out[17] that these normalized magnetization curves for hard (Bean) superconductors with $n\gg1$ differ very little for various geometries; between thin strips[6] and thin circular disks[7–9] the difference is <0.011, and between thin circular and quadratic disks the difference is <0.002.[26] Similarly, we find that for our rectangular bars the normalized $M(h)$ for various ratios b/a differs by <0.03 from some average curve $M(h)$.

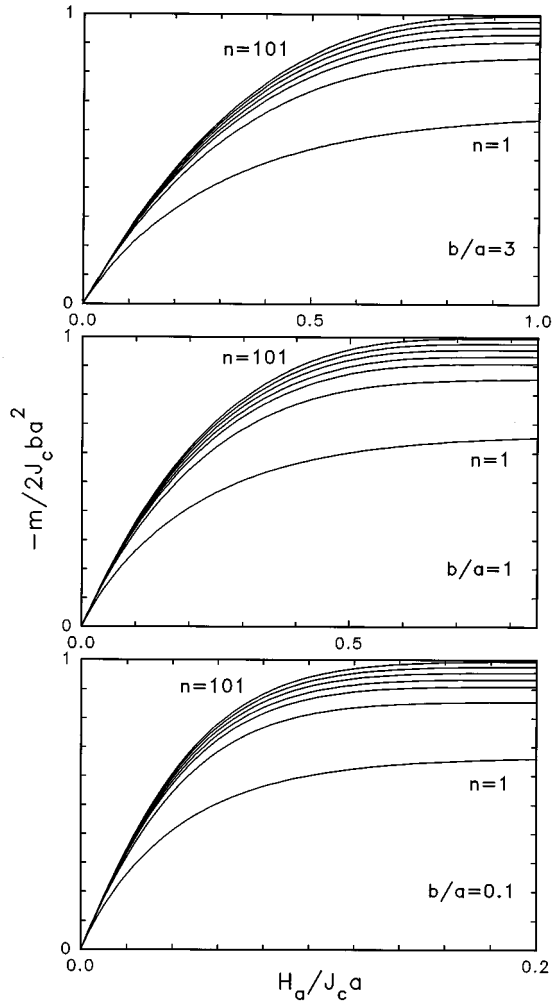

FIG. 17. Virgin magnetization curves $m(H_a)$ of rectangular bars with side ratios $b/a=3$, 1, and 0.1 (from top to bottom) and creep exponents $n=1$, 3, 5, 7, 11, 21, and 101 in the current-voltage law $E\propto J^n$.

Figure 16 shows normalized magnetization curves for $b/a=6$ to 0.005. All these curves are very similar. To avoid that they merge into one bold line, each curve is slightly shifted horizontally. For $b/a\leqslant0.02$ the computed $M(h)$ practically coincides with the thin strip result[11] $M(h)=\tanh(h)$. The parallel Bean limit $M(h)=h-h^2/4$ is reached only at relatively large side ratios $b/a\gg6$, which are difficult to compute. Since the contribution to $M(h)$ from the two end regions $y\approx\pm b$ is additive, one may conclude that for $b\gg a$ the difference $M(h)-h+h^2/4$ is proportional to a/b.

Figure 17 shows virgin magnetization curves $m(H_a)$ for various creep exponents $n=1$, 3, 5, 7, 11, 21, and 101 for bars with side ratios $b/a=3$, 1, and 0.1 in constantly ramped perpendicular field. In these plots the ramp rate was

$\dot{B}_a = E_c/a$, but different ramp rates give identical curves with scaled axes; this scaling may be found by choosing different E_c and J_c values in $E = E_c(J/J_c)^n$ keeping the ratio E_c/J_c^n constant. Except for the ohmic case $n=1$, the curves for $n \geqslant 3$ practically collapse into one bold line if m is multiplied by $(n+1/2)/n$, which means normalization to unity saturation value, cf. Eq. (69), without changing the abscissa H_a. This means the exponent n or activation energy U discussed following Eq. (1), cannot be determined from an experiment with constantly ramped $H_a(t)$. However, the exponent n strongly influences the creep rate during constant-held H_a (Sec. IV B) and also the shape of the magnetization loops, in particular when $H_a(t)$ is swept sinusoidally.

For the Bean limit $n \to \infty$, $J_c = \text{const}$, the entire magnetization loop $m_{\downarrow\uparrow}(H_a)$ during field sweep between $+H_0$ and $-H_0$ can be obtained from the above virgin magnetization curve $m(H_a)$ by the prescription[2,6,8,9]

$$m_{\downarrow}(H_a) = m(H_0) - 2m\left(\frac{H_0 - H_a}{2}\right) \tag{78}$$

and $m_{\uparrow}(H_a) = -m_{\downarrow}(-H_a)$, where the arrows denote increasing and decreasing $H_a(t)$, cf. Eq. (72).

VI. CONCLUDING REMARKS

The presented method for the computation of flux and current penetration into bars or disks circumvents the costly computation of the magnetic field in the infinite space and its inaccurate spatial differentiation. Instead, the current density $J(x,y,t)$ *inside the bar* is obtained *directly* by time integration of a 2D integral equation of motion, without requiring any differentiation. The main *theoretical* problem was the incorporation of the time dependent applied magnetic field $H_a(t)$ into this equation, since any spatial differentiation makes this term vanish. The solution to this principal problem is that the ''outer world'' (i.e., H_a) enters the equation of motion (7) or (24) in form of the induced surface current (74), which penetrates into the conductor by nonlinear diffusion. A further problem is the optimum choice of the cutoff in the diagonal terms Q_{ii} of the matrix $Q_{ij} = (1/2\pi)\ln|\mathbf{r}_i - \mathbf{r}_j|$; the Q_{ij} may be interpreted as the mutual and self-inductances of double strips.[52] A main *practical* problem might be the required inversion of the $N \times N$ matrix Q_{ij}, but this inversion has to be performed only once for a given grid at the beginning of the computation; for $N \leqslant 1000$ it presents no problem even on a personal computer.

In this paper the superconductor is modeled as a nonlinear conductor with general current-voltage law $E = E(J)$, or a power law $E \propto J^n$, or with linear complex resistivity $\rho_{ac}(\omega) = E/J$. Numerous useful formulas are presented in Sec. IV, which may be used to compute magnetization curves, field and current profiles, creep, the linear ac response, and flux penetration in the Meissner state. The universality of flux creep is demonstrated in Sec. IV B and in Ref. 49. It appears that the power law $E \propto J^n$ is distinguished since it allows for exact separation of the variables $\mathbf{r}$ and t during creep and it has the required physical property $E \to 0$ for $J \to 0$, in contrast to the other separable model $E \propto \exp(J/J_1)$.

In Sec. V we have presented mainly Bean-like results for large creep exponents $n \gg 1$, but most of the given formulae apply to any $n \geqslant 1$; in fact the computation is easiest for small n. More details on the magnetization curves with stronger creep (smaller n) for bars and disks or cylinders will be published elsewhere.[43] If desired, with the presented method the magnetization and flux and current profiles are easily calculated also for non-Bean models with field dependent $J_c(B)$ and $n(B)$ and for other than rectangular specimen cross sections. The obtained flux- and current-free zones of the Bean model differ from the concentric ellipsoids assumed in Refs. 4 and 5.

ACKNOWLEDGMENTS

I acknowledge useful discussions with M. V. Indenbom, A. Gurevich, L. Prigozhin, A. Forkl, Th. Schuster, H. Kuhn, Ch. Jooss, Yu. N. Ovchinnikov, A. M. Campbell, L. Burlachkov, J. R. Clem, and J. Gilchrist.

[1] C. P. Bean, Phys. Rev. Lett. **8**, 250 (1962); Rev. Mod. Phys. **36**, 31 (1964).

[2] A. M. Campbell and J. E. Evetts, Adv. Phys. **21**, 199 (1972).

[3] S. Senoussi, J. Phys. III (Paris) **2**, 1041 (1992); M. E. McHenry and R. A. Sutton, Prog. Mater. Sci. **38**, 159 (1994).

[4] V. M. Krasnov, V. A. Larkin, and V. V. Ryazanov, Physica C **174**, 440 (1991).

[5] K. V. Bhagwat and P. Chaddah, Physica C **190**, 444 (1992); **224**, 155 (1994).

[6] A. Forkl and H. Kronmüller, Physica C **228**, 1 (1994); Phys. Rev. B **52**, 16 130 (1995).

[7] P. N. Mikheenko and Yu. E. Kuzovlev, Physica C **204**, 229 (1993).

[8] J. Zhu, J. Mester, J. Lockhart, and J. Turneaure, Physica C **212**, 216 (1993).

[9] J. R. Clem and A. Sanchez, Phys. Rev. B **50**, 9355 (1994).

[10] W. T. Norris, J. Phys. D **3**, 489 (1970); Y. Yang, T. Hughes, C. Beduz, D. M. Spiller, R. G. Scurlock, and W. T. Norris, Physica C **256**, 378 (1996).

[11] E. H. Brandt, M. Indenbom, and A. Forkl, Europhys. Lett. **22**, 735 (1993); E. H. Brandt and M. Indenbom, Phys. Rev. B **48**, 12 893 (1993).

[12] E. Zeldov, J. R. Clem, M. McElfresh, and M. Darwin, Phys. Rev. B **49**, 9802 (1994).

[13] E. H. Brandt, Phys. Rev. B **49**, 9024 (1994); Phys. Rev. Lett. **71**, 2821 (1993).

[14] A. T. Dorsey, Phys. Rev. B **51**, 15 329 (1995).

[15] E. H. Brandt, Phys. Rev. B **50**, 4034 (1994).

[16] P. H. Kes, J. Aarts, J. van der Berg, C. J. van der Beek, and J. A. Mydosh, Supercond. Sci. Technol. **1**, 242 (1989).

[17] J. Gilchrist, Physica C **219**, 67 (1994).

[18] E. Zeldov, A. I. Larkin, V. B. Geshkenbein, M. Konczykowski, D. Majer, B. Khaykovich, V. M. Vinokur, and H. Strikhman, Phys. Rev. Lett. **73**, 1428 (1994); E. Zeldov *et al.*, Physica C

235-240, 2761 (1994); N. Morozov, E. Zeldov, D. Majer, and B. Khaykovich, Phys. Rev. Lett. **76**, 138 (1996); I. L. Maksimov and A. A. Elistratov, Pis'ma Zh. Eksp. Teor. Fiz. **61**, 204 (1995) [JETP Lett. **61**, 208 (1995)].

[19] M. Benkraouda and J. R. Clem, Phys. Rev. B **53**, 5716 (1996); J. R. Clem, R. P. Huebener, and D. E. Gallus, J. Low Temp. Phys. **5**, 449 (1973); W. Buck, K.-P. Selig, and J. Parisi, *ibid.* **45**, 21 (1981); J. Provost, E. Paumier, and A. Fortini, J. Phys. F **4**, 439 (1974).

[20] E. H. Brandt, Physica C **235-240**, 2939 (1994).

[21] Th. Schuster, H. Kuhn, E. H. Brandt, M. Indenbom, M. V. Koblischka, and M. Konczykowski, Phys. Rev. B **50**, 16 684 (1994).

[22] Th. Schuster, M. V. Indenbom, H. Kuhn, E. H. Brandt, and M. Konczykowski, Phys. Rev. Lett. **73**, 1424 (1994).

[23] Th. Schuster, H. Kuhn, E. H. Brandt, M. V. Indenbom, M. Kläser, G. Müller-Vogt, H.-U. Habermeier, H. Kronmüller, and A. Forkl, Phys. Rev. B **52**, 10 375 (1995); Th. Schuster, H. Kuhn, and E. H. Brandt, Phys. Rev. B **54**, 3514 (1996).

[24] E. H. Brandt, Phys. Rev. Lett. **74**, 3025 (1995).

[25] E. H. Brandt, Phys. Rev. Lett. **52**, 15 442 (1995).

[26] E. H. Brandt, Rep. Prog. Phys. **58**, 1465 (1995).

[27] H. Theuss, A. Forkl, and H. Kronmüller, Physica C **190**, 345 (1992); R. L. Prozorov, A. A. Polyanskii, V. I. Nikitenko, I. V. Grekhov, L. A. Delimova, and I. A. Liniichuk, Sverkhprovodimost' **6**, 1714 (1993) [Supercond. Phys. Chem. Technol. **6**, 563 (1993)]; A. A. Polyanskii, A. Gurevich, A. E. Pashitski, N. F. Heinig, R. D. Redwing, J. E. Norman, and D. C. Larbalestier, Phys. Rev. B **53**, 8687 (1996).

[28] P. D. Grant, M. W. Denhoff, W. Xing, P. Brown, S. Govorkov, J. C. Irwin, B. Heinrich, H. Zhou, A. A. Fife, and A. R. Cragg, Physica C **229**, 289 (1994); W. Xing, B. Heinrich, Hu Zhou, A. A. Fife, and A. R. Cragg, J. Appl. Phys. **76**, 4244 (1994).

[29] E. H. Brandt, Phys. Rev. B **46**, 8628 (1992); R. J. Wijngaarden, H. J. W. Spoelder, R. Surdeanu, and R. Griessen, Phys. Rev. B (to be published); Ch. Jooss, R. Warthmann, A. Forkl, H.-U. Habermeier, B. Leibold, and H. Kronmüller, Physica C (to be published).

[30] J. R. Clem, H. R. Kerchner, and T. S. Sekula, Phys. Rev. B **14**, 1893 (1976).

[31] E. H. Brandt, Phys. Rev. B **50**, 13 833 (1994).

[32] J. Kötzler, G. Nakielski, M. Baumann, R. Behr, F. Goerke, and E. H. Brandt, Phys. Rev. B **50**, 3384 (1994).

[33] A. Gurevich and H. Küpfer, Phys. Rev. B **48**, 6477 (1993).

[34] A. Gurevich, Int. J. Mod. Phys. B **9**, 1045 (1995).

[35] A. Gurevich and E. H. Brandt, Phys. Rev. Lett. **73**, 178 (1994).

[36] Th. Schuster, H. Kuhn, and E. H. Brandt, Phys. Rev. B **51**, 697 (1995).

[37] V. B. Geshkenbein, M. V. Feigel'man, and V. M. Vinokur, Physica C **185-189**, 2511 (1991).

[38] E. H. Brandt and A. Gurevich, Phys. Rev. Lett. **75**, 1723 (1996).

[39] M. A. Skvortsov and V. B. Geshkenbein, Zh. Eksp. Teor. Fiz. **105**, 1379 (1994) [Sov. Phys. JETP **78**, 743 (1994)].

[40] E. M. Parvin, A. Singfield, W. F. Vinen, and G. F. Cox, Supercond. Sci. Technol. **6**, 5252 (1993).

[41] M. Daeumling and D. C. Larbalestier, Phys. Rev. B **40**, 9350 (1989); D. J. Frankel, J. Appl. Phys. **50**, 5402 (1979).

[42] L. W. Conner and A. P. Malozemoff, Phys. Rev. B **43**, 402 (1991).

[43] E. H. Brandt (unpublished).

[44] V. M. Vinokur, M. V. Feigel'man, and V. B. Geshkenbein, Phys. Rev. Lett. **67**, 915 (1991).

[45] J. Rhyner, Physica C **212**, 292 (1993).

[46] J. Gilchrist and C. J. van der Beek, Physica C **231**, 147 (1994).

[47] M. V. Indenbom and E. H. Brandt, Phys. Rev. Lett. **73**, 1731 (1994); M. V. Indenbom, H. Kronmüller, T. W. Li, P. H. Kes, and A. A. Menovsky, Physica C **22**, 203 (1994).

[48] M. V. Indenbom, Th. Schuster, H. Kuhn, H. Kronmüller, T. W. Li, and A. A. Menovsky, Phys. Rev. B **51**, 15 484 (1995).

[49] E. H. Brandt, Phys. Rev. Lett. **76**, 4030 (1996).

[50] E. H. Brandt, Phys. Rev. B **48**, 6699 (1993).

[51] I. M. Ryzhik and I. S. Gradshteyn, *Tables of Integrals, Series and Products* (Academic Press, New York, 1965).

[52] J. Gilchrist and E. H. Brandt, Phys. Rev. B **54**, 3530 (1996).

[53] M. Coffey and J. R. Clem, Phys. Rev. B **67**, 386 (1991).

[54] E. H. Brandt, Phys. Rev. B **67**, 2219 (1991).

[55] A. E. Koshelev and V. M. Vinokur, Physica C **173**, 465 (1991).

[56] D. S. Fisher, M. P. A. Fisher, and D. A. Huse, Phys. Rev. B **43**, 130 (1991).

[57] A. T. Dorsey, Phys. Rev. B **43**, 7575 (1991).

[58] G. Blatter, M. V. Feigel'man, V. B. Geshkenbein, A. I. Larkin, and V. M. Vinokur, Rev. Mod. Phys. **66**, 1125 (1994).

[59] A. Forkl, Phys. Scr. **T49**, 148 (1993).

[60] Th. Schuster, M. V. Indenbom, M. R. Koblischka, H. Kuhn, and H. Kronmüller, Phys. Rev. B **49**, 3443 (1994).

[61] L. Prigozhin, Eur. J. Appl. Math. **7**, 237 (1996); Free Boundary Problems Newsletter **10**, 2 (1996); J. Comput. Phys. (to be published).

[62] Th. Becker, R. Warthmann, Ch. Jooss, and H. Kronmüller (unpublished).

[63] M. Ashkin, J. Appl. Phys. **50**, 7060 (1979).

[64] V. B. Zenkevich, V. V. Zheltov, and A. S. Romanyuk, Dokl. Akad. Nauk SSSR **251**, 339 (1980) [Sov. Phys. Dokl. **25**, 210 (1980)].

[65] R. Navarro and L. J. Campbell, Supercond. Sci. Technol. **5**, S200 (1992).

[66] K. L. Telschow and L. S. Koo, Phys. Rev. B **50**, 6923 (1994).